

Euler-Euler Multiphase CFD-Simulation with Full Reynolds Stress Model and Anisotropic Bubble-induced Turbulence

Parekh, J.; Rzehak, R.;

Originally published:

October 2017

International Journal of Multiphase Flow 99(2018), 231-245

DOI: <https://doi.org/10.1016/j.ijmultiphaseflow.2017.10.012>

Perma-Link to Publication Repository of HZDR:

<https://www.hzdr.de/publications/Publ-25730>

Release of the secondary publication
on the basis of the German Copyright Law § 38 Section 4.

CC BY-NC-ND

Euler-Euler Multiphase CFD-Simulation with Full Reynolds Stress Model and Anisotropic Bubble-induced Turbulence

Jigar Parekh, Roland Rzehak^{*}

Helmholtz-Zentrum Dresden – Rossendorf, Institute of Fluid Dynamics,
Bautzner Landstrasse 400, D-01328 Dresden, Germany

Abstract

In the present work, Euler-Euler modeling of bubbly flows is combined with a full Reynolds stress model for the turbulence in the liquid carrier phase. Reynolds stress models have only rarely been explored in this context, although effects requiring this level of description are frequently encountered in industrial applications towards which the Euler-Euler approach is geared. In particular, source terms describing the additional bubble-induced contribution to the liquid phase turbulence with proper account for its anisotropy have not firmly been established yet. A formulation based on the direction of bubble motion relative to the liquid is given here. Two well-known variants of Reynolds stress models due to Launder, Reece and Rodi and Speziale, Sarkar and Gatski are compared. Closure relations for the bubble forces are applied that have been shown previously to work well over a range of conditions. The model is validated by comparison with a set of pipe flow data that contains variations of liquid and gas flow rates as well as different pipe diameters. An important criterion for the selection of the data was to provide measurements of individual components of the Reynolds stress tensor.

Keywords: dispersed gas liquid multiphase flow, Euler-Euler two-fluid model, Reynolds stress turbulence model, bubble-induced turbulence, CFD simulation, model validation

^{*} Corresponding author. E-mail: r.rzehak@hzdr.de

TABLE OF CONTENTS

1	INTRODUCTION	3
2	DESCRIPTION OF MODELS.....	5
2.1	Two-phase conservation equations.....	5
2.2	Turbulence modeling	6
2.2.1	SST turbulence Model	7
2.2.2	Reynolds stress models (RSMs)	8
2.2.3	Source terms for bubble-induced turbulence	11
2.2.4	Turbulent Wall Function.....	13
2.3	Interfacial forces.....	14
3	SUMMARY OF EXPERIMENTAL DATA	18
3.1	Tests from Hosokawa et al. (2009, 2010)	18
3.2	Tests from Liu (1998)	18
3.3	Tests from Shawkat et al. (2008)	19
4	SIMULATION RESULTS	21
4.1	Tests of Hosokawa et al. (2009, 2010).....	23
4.2	Tests from Liu (1998)	27
4.3	Tests from Shawkat et al. (2008)	29
5	DISCUSSION AND CONCLUSIONS	32
6	ACKNOWLEDGEMENT	33
7	NOMENCLATURE	33
8	REFERENCES	35

1 INTRODUCTION

Bubbly flows are common in many engineering disciplines ranging from chemical engineering and biotechnology to energy and transportation. In such systems, the exchange of momentum, heat, and mass between the phases poses a complex multiphysics problem. Accordingly, design and optimization of technical equipment present a great challenge. In this situation, CFD simulations bear the potential of identifying energy- and resource-efficient solutions which are prohibitively expensive and time-consuming to uncover by conventional semi-empirical methods.

CFD simulations of dispersed bubbly flow on the scale of technical equipment become feasible within the Eulerian two-fluid framework of interpenetrating continua. In the past, this type of multiphase flow modeling has mostly been combined with two-equation models for the turbulence in the liquid carrier phase (e.g. Lee et al. 1989, Sokolichin and Eigenberger 1999). However, even for single-phase flows the applicability of these models is restricted to simple geometries like pipe flow by the assumption of isotropic turbulent fluctuations. In particular they cannot describe flows with secondary motions of Prandtl's second kind or boundary layer separation as well as effects of swirl or streamline curvature (Wilcox 2006, ch 6.2), which arise frequently in technical applications with complex geometries. Full Reynolds stress turbulence models can overcome these deficiencies and cover much more general flow situations, but have only rarely been applied in the context of multiphase flows. A particular necessity in this context is to include the bubble-induced contribution to turbulence by means of appropriate source terms in the turbulence model (e.g. Troshko and Hassan 2001, Politano et al. 2003). To retain the full advantage of the capability to represent anisotropic Reynolds stresses, these source terms should account for the anisotropy of the bubble-induced turbulence as well.

Early attempts combining Euler-Euler simulations with Reynolds stress models (RSMs) are the works of Lopez de Bertodano et al. (1990) and Lahey et al. (1993). The RSM of Launder et al. (1975) and an explicit algebraic RSM originally due to Rodi (1976), respectively, were used as the base models. An anisotropic bubble-induced contribution to the turbulence was included by means of source terms in the turbulence model equations. All models were implemented in the NPHASE code. Flows in ducts of different cross-sections were considered as applications. More recently, Mimouni et al. (2009) applied the RSM of Launder et al. (1975) to flow in a straight pipe and a pipe with a sudden expansion using the NEPTUNE code. Bubble-induced turbulence was neglected. Comparison with the standard k - ϵ model was made. Different turbulence models including RSMs were compared for flows in bubble columns by Ekambara and Dhotre (2010), Silva et al. (2012), and Masood et al. (2014). The first two of these made use of the RSM of Speziale et al. (1991), the latter employed the explicit algebraic RSM of Wallin and Johansson (2000), all as implemented in the code ANSYS CFX. Comparison was made with various two-equation models and in Ekambara and Dhotre (2010) also with LES. The bubble-induced contribution to turbulence was not included directly, only its effect on the mean flow was taken into account by an increased turbulent viscosity according to Sato et al. (1981). Finally, Colombo and Fairweather (2015) applied both the RSMs of Launder et al. (1975) and Speziale et al. (1991) with anisotropic source terms for the bubble-induced turbulence to a rather large database of bubbly pipe flows. Comparison was made with the standard k - ϵ model using isotropic

source terms for the bubble-induced turbulence. The simulations were made with StarCCM+.

From the literature overview given above it becomes clear that definite results on the form of suitable anisotropic source terms to describe the bubble-induced turbulence are still lacking. Previous works that included such source terms alluded to an inviscid cell-averaging calculation (Arnold et al. 1988). Since the bubble-induced turbulence is usually associated with bubble wakes (e.g. Riboux et al. 2013) which cannot be captured by inviscid theory, this form appears rather questionable. A better supported form can be derived from the recent experiments of Hosokawa and Tomiyama (2013) who measured fluctuations in different coordinate directions in a flow where the bubble-induced turbulence dominates. A further consideration that has not been paid due attention in the previous works is that for a generally applicable model, the anisotropy must be tied to the direction of bubble motion. Alignment of bubble motion with a particular coordinate axis is specific to certain flow configurations and depends on the choice of coordinate frame. Hence, defining the anisotropy of the bubble-induced turbulence in a fixed coordinate system obviously does not correctly capture the underlying physics. New anisotropic source terms to model the bubble-induced turbulence based on these ideas are proposed in section 2.2.3.

In addition, the question which of the many different proposed RSMs constitutes a good general-purpose choice remains open, much like for single-phase flows. According to their widespread use, the models of Launder et al. (1975) and Speziale et al. (1991) are chosen for the present investigation. Calculations based on the SST model are provided for comparison. A complete description of the equations for all applied turbulence models is given in sections 2.2.1 and 2.2.2.

Of course, comparison between simulation and experiment also depends on all other aspects of the overall model besides turbulence. As a common starting point, a baseline model has been developed and validated for a large number of applications (Rzehak and Krepper 2013, 2013a, 2015, Ziegenhein et al. 2015, 2017, Liao et al. 2016, Rzehak et al. 2017, 2017a). This model has also been implemented in OpenFOAM (Rzehak and Kriebitzsch 2015, Kriebitzsch and Rzehak 2016). For the sake of completeness, a brief description is provided in section 2.

RSMs introduce a significant number of further variables, namely six independent components of the Reynolds stress tensor instead of only the turbulent kinetic energy. Therefore, the foremost consideration in selecting suitable experimental data for model validation is that they should provide measurements of individual Reynolds stress components. Like in a previous investigation of bubble-induced turbulence in the frame of two-equation models (Rzehak and Krepper 2013b), experiments on bubbly flow in pipes of different diameter $D \approx 25, 50, 200$ mm are used herein, taken from the works of Hosokawa and Tomiyama 2010, Liu 1998, and Shawkat et al. 2008, respectively. The first of these, represents an extension of the earlier work Hosokawa and Tomiyama (2009) providing data on four individual Reynolds stress components rather than just turbulent kinetic energy. The latter two contain data on a single and two of the normal components, respectively. An overview of these measurements is given in section 3.

The setup of the simulations and the comparison of their results with the experimental data are finally presented in section 4 while a discussion and conclusions are offered in section 5.

2 DESCRIPTION OF MODELS

2.1 Two-phase conservation equations

Detailed discussions and derivations of the conservation equations for two-phase flow can be found in various recent monographs (e.g. Drew and Passman 1998, Yeoh and Tu 2010, Ishii and Hibiki 2011). Therefore, here only a brief summary of the relevant background is given.

Using the index $k = L, G$ to denote the liquid and gas phase, respectively, the phasic continuity equations read

$$\frac{\partial}{\partial t}(\alpha_k \rho_k) + \nabla \cdot (\alpha_k \rho_k \mathbf{u}_k) = 0, \quad (1)$$

while the phasic momentum equations are

$$\frac{\partial}{\partial t}(\alpha_k \rho_k \mathbf{u}_k) + \nabla \cdot (\alpha_k \rho_k \mathbf{u}_k \otimes \mathbf{u}_k) = -\alpha_k \nabla p_k + \nabla \cdot (\alpha_k \mathbf{T}_k) + \mathbf{F}_k. \quad (2)$$

In Eq. (2), p is the pressure and \mathbf{T} denotes the stress tensor, which includes both viscous and turbulent stresses. Using Stokes' hypothesis for the second coefficient of viscosity (White 1992), it can be described as

$$\mathbf{T}_k = 2 \mu_k^{mol} \left(\mathbf{D}_k - \frac{1}{3} \text{tr}(\mathbf{D}_k) \mathbf{I} \right) - \rho_k \mathbf{R}_k, \quad (3)$$

where \mathbf{I} is the unit tensor, \mathbf{D} is the strain rate tensor

$$\mathbf{D}_k = \frac{1}{2} (\nabla \mathbf{u}_k + (\nabla \mathbf{u}_k)^T), \quad (4)$$

and μ^{mol} is the molecular dynamic viscosity. \mathbf{R} is the Reynolds stress tensor which is defined in terms of the turbulent fluctuating velocities \mathbf{u}'_L as $\mathbf{R}_k = \langle \mathbf{u}'_k \otimes \mathbf{u}'_k \rangle$. It can be modeled either by using the Boussinesq eddy viscosity hypothesis (see Section 2.2.1) or by solving the Reynolds stress transport equation (see Section 2.2.2).

The term \mathbf{F}_i in Eq. (2) accounts for the forces on the k^{th} phase and consists of the body forces and the interfacial forces. The only body force considered here is the gravitational force. The interfacial forces comprise the drag force and the non-drag forces, which are explained in more detail in Section 2.3:

$$\mathbf{F}_k = \mathbf{F}_k^{body} + \mathbf{F}_k^{inter} = \alpha_k \rho_k \mathbf{g} + \mathbf{F}_k^{inter}. \quad (5)$$

Further relations needed to obtain a complete system of equations are expressions for the overall conservation of volume,

$$\sum_{k=L,G} \alpha_k = 1, \quad (6)$$

and momentum,

$$\mathbf{F}_L^{inter} = -\mathbf{F}_G^{inter}, \quad (7)$$

as well as a relation between the pressures, where an equilibrium pressure state is assumed here, i.e.

$$p_G = p_L = p. \quad (8)$$

Finally, a thermal equation of state is required for each phase, which relates pressure, temperature, and density as

$$\rho_k = \rho_k(p_k, T_k). \quad (9)$$

If both phases are considered to be incompressible, no equation of state is needed and the density becomes just a fixed parameter with pressure acting as a Lagrange multiplier enforcing the incompressibility constraint for the mixture velocity $\mathbf{u}_{mix} = \sum_{k=L,G} \alpha_k \mathbf{u}_k$, i.e. $\nabla \cdot \mathbf{u}_{mix} = 0$. However, the velocities of the individual phases need not be divergence-free.

2.2 Turbulence modeling

Because of the low density and small spatial scales of the dispersed phase, for bubbly flows it is sufficient to consider only the turbulence in the continuous phase. Therefore the index ' L ' is dropped throughout this section for notational convenience. Two contributions to the turbulent fluctuations have to be taken into account, a shear-induced turbulence and a bubble-induced turbulence (BIT). The latter one is included by adding suitable source terms to common turbulence models, which are known to give a good description of single-phase flows where only the former one occurs.

A two-equation turbulence model that is known to perform well for many technically relevant single-phase flows is provided by the SST model (Menter, 2009). Therefore, this was used in previous work and is taken here as a reference. Details of this model are given in section 2.2.1. The selection as to which of the many different existing RSMs should be used has again been based on the available experiences for single-phase flows. Two variants that have been frequently applied with good success have emerged from the works of Launder, Reece, and Rodi (LRR, Launder et al. 1975) and Speziale, Sarkar, and Gatski (SSG, Speziale et al. 1991). A description of these basic turbulence models is given in section 2.2.2.

For use with the isotropic SST model, isotropic source terms describing the bubble-induced contribution to the turbulence have been proposed (Rzehak and Krepper 2013, 2013b). To take advantage of the capabilities to describe anisotropic turbulent fluctuations, new anisotropic source terms are developed here by a suitable splitting of the turbulent energy due to the bubbles. Care has been taken to obtain a coordinate-frame invariant formulation that accounts for the direction of the motion of the bubbles relative to the liquid. Both isotropic and anisotropic source terms are described in detail in section 2.2.3.

Resolving the viscous sub-layer near the solid walls is avoided using turbulent wall functions. These are currently taken the same as in single-phase flow. For use with the SST model a compound wall function is available, which is valid in both the logarithmic and the viscous sublayer. For use with the RSMs such a rather sophisticated treatment is not known, and hence a simpler formulation is applied at present, keeping the focus on the inclusion of the BIT. The wall function treatment is discussed in section 2.2.4 below.

2.2.1 SST turbulence Model

In the SST model (Menter, 2009), the k - ω and the k - ε models are combined with a blending function in such a way that the respective advantages of the k - ω model (in the vicinity of the wall) and the k - ε model (in free flow region) are taken advantage of. Usually, k and ω are employed as independent variables, the equation for ε being transformed into an equivalent equation for ω . This transformed equation contains a cross-diffusion term which is not present in the usual ω -equation. Therefore, the equations for turbulent kinetic energy k and turbulent frequency ω are:

$$\frac{\partial}{\partial t}(\alpha \rho k) + \nabla \cdot (\alpha \rho \mathbf{u} k) = \nabla \cdot (\alpha (\mu^{mol} + \sigma_k^{-1} \mu^{turb}) \nabla k) + \alpha (P - C_\mu \rho \omega k) + S^k \quad (10)$$

$$\begin{aligned} \frac{\partial}{\partial t}(\alpha \rho \omega) + \nabla \cdot (\alpha \rho \mathbf{u} \omega) = & \nabla \cdot (\alpha (\mu^{mol} + \sigma_\omega^{-1} \mu^{turb}) \nabla \omega) \\ & + \alpha \left(C_{\omega P} \frac{\rho P}{\mu^{turb}} - C_{\omega D} \rho \omega^2 \right) \\ & + 2\alpha \sigma_{\omega 2}^{-1} \rho (1 - F_1) \frac{\nabla k \cdot \nabla \omega}{\omega} + S^\omega \end{aligned} \quad (11)$$

Here F_1 denotes the blending function which assumes a value of one for the k - ω model and zero for the k - ε model. It is defined as

$$F_1 = \tanh \left[\left(\min \left(\max \left(\frac{\sqrt{k}}{C_\mu \omega y}, \frac{500 \mu^{mol}}{\rho \omega y^2} \right), \frac{4 \sigma_{\omega 2}^{-1} \rho k}{y^2 \max \left(\frac{2}{\sigma_{\omega 2}} \rho \frac{\nabla k \cdot \nabla \omega}{\omega}, 1.0 \cdot 10^{-10} \right)} \right) \right)^4 \right], \quad (12)$$

where y is the distance normal to the wall.

The model constants $C_\mu, C_{\omega P}, C_{\omega D}, \sigma_k^{-1}$ and σ_ω^{-1} , are also interpolated between the corresponding values of the k - ω model (index '1') and k - ε model (index '2') using the blending function F_1 as

$$\chi = F_1 \chi_1 + (1 - F_1) \chi_2. \quad (13)$$

Values of the above constants are taken as usual for single-phase flows. A summary is given in Table 1. Note that these values deviate slightly from those commonly used for the k - ω and k - ε models alone (NASA, 2014).

	C_μ	$C_{\omega P}$	$C_{\omega D}$	σ_k^{-1}	σ_ω^{-1}
k- ω model (index '1')	0.09	0.5532	0.075	0.85034	2.0
k- ε model (index '2')	0.09	0.4463	0.0828	1.0	0.85616

Table 1 Parameter values for the k - ω and k - ε models.

The production of turbulence is given in terms of the strain rate tensor as defined in Eq. (4), including a limiter to prevent the build-up of turbulent kinetic energy in stagnation zones, as

$$P = \min(2\mu^{turb} \mathbf{D} : \nabla \mathbf{u}, 10C_\mu \rho \omega k). \quad (14)$$

Since bubble-induced effects are already contained in k and ω due to the added source terms S^k and S^ω (see section 2.2.3), the turbulent viscosity is evaluated from the standard relation of the SST model, which includes a limiter based on the generalized shear rate $\gamma = \sqrt{2\mathbf{D}:\mathbf{D}}$, i.e.

$$\mu^{turb} = \frac{\rho k}{\max(\omega, C_\gamma F_2 \gamma)}, \quad (15)$$

where F_2 is a second blending function defined as

$$F_2 = \tanh \left[\left(\max \left(\frac{2\sqrt{k}}{C_\mu \omega y}, \frac{500\mu^{mol}}{\rho \omega y^2} \right) \right)^2 \right] \quad (16)$$

and $C_\gamma = 1/0.31$ is a further model constant.

The Reynolds stress tensor \mathbf{R} is then given by

$$-\rho \mathbf{R} = 2\mu^{turb} \left(\mathbf{D} - \frac{1}{3} \text{tr}(\mathbf{D}) \mathbf{I} \right) - \left(\frac{2}{3} \rho k \right) \mathbf{I}. \quad (17)$$

2.2.2 Reynolds stress models (RSMs)

The transport equation for the Reynolds stress tensor $\mathbf{R} = \langle \mathbf{u}' \otimes \mathbf{u}' \rangle$ is given as

$$\begin{aligned} \frac{\partial}{\partial t}(\alpha \rho \mathbf{R}) + \nabla \cdot (\alpha \rho \mathbf{u} \otimes \mathbf{R}) = & \nabla \cdot (\alpha (\mu^{mol} + C_s \mu^{turb}) \nabla \otimes \mathbf{R}) \\ & + \alpha \rho \left(\mathbf{P} + \boldsymbol{\Phi} - \frac{2}{3} \epsilon \mathbf{I} \right) + \mathbf{S}^R, \end{aligned} \quad (18)$$

and that for the turbulent dissipation rate ϵ_L as

$$\begin{aligned} \frac{\partial}{\partial t}(\alpha \rho \epsilon) + \nabla \cdot (\alpha \rho \mathbf{u} \epsilon) = & \nabla \cdot (\alpha (\mu^{mol} + C_\epsilon \mu^{turb}) \cdot \nabla \epsilon) \\ & + \alpha \rho \frac{\epsilon}{k} \left(C_{\epsilon,1} \frac{1}{2} \text{tr}(\mathbf{P}) - C_{\epsilon,2} \epsilon \right) + S^\epsilon. \end{aligned} \quad (19)$$

Here, \mathbf{S}^R and S^ϵ are the source terms added to the single-phase model to include the BIT. The other terms on the right side of both equations are the well-known ones (e.g. Wilcox 2006, ch 6.3) describing diffusion, production by mean strain, pressure-strain correlation, and dissipation to be discussed in more detail after giving some further definitions.

The turbulent kinetic energy is related to the Reynolds stress by $k = \frac{1}{2} \text{tr}(\mathbf{R})$. In contrast to the k - ω SST model, the turbulent viscosity in RSMs is anisotropic. Thus tensor forms of molecular and turbulent viscosities are defined as

$$\mu^{mol} = \mu^{mol} \mathbf{I}, \quad (20)$$

$$\mu^{turb} = \frac{\rho k}{\epsilon} \mathbf{R}. \quad (21)$$

The anisotropy of the Reynolds stresses is expressed by the so-called anisotropy tensor \mathbf{A} with components[†]

[†] Sometimes a definition appears in the literature which is twice the one given here.

$$A_{ij} = \frac{R_{ij} - \frac{1}{3} R_{kk} \delta_{ij}}{R_{ll}} = \frac{R_{ij}}{2k} - \frac{1}{3} \delta_{ij}, \quad (22)$$

where $i, j = x, y, z$ and summation over repeated indices is implied.

Components of strain and the rotation rate tensors D_{ij} and Ω_{ij} are given by

$$D_{ij} = \frac{1}{2} \left(\frac{\partial u_i}{\partial x_j} + \frac{\partial u_j}{\partial x_i} \right), \quad (23)$$

$$\Omega_{ij} = \frac{1}{2} \left(\frac{\partial u_i}{\partial x_j} - \frac{\partial u_j}{\partial x_i} \right). \quad (24)$$

The Reynolds stress diffusion (first term on the right in Eq. (18)) is modeled according to Daly and Harlow (1970), which was considered as a simplified version in the work of Launder et al. (1975). The value of the coefficient C_s given in Table 2 below is taken from Launder et al. (1975).

The turbulent production of Reynolds stress (second term on the right in Eq. (18)) is represented exactly and given by

$$\mathbf{P} = -(\mathbf{R} \cdot \nabla \mathbf{u}) + (\mathbf{R} \cdot \nabla \mathbf{u})^T. \quad (25)$$

Note that the production of turbulent kinetic energy is given by $\frac{1}{2} \text{tr}(\mathbf{P})$.

Much of previous modeling work has concentrated on the pressure-strain correlation (third term on the right in Eq. (18)), which accounts for the redistribution of energy amongst the Reynolds stress components due to pressure fluctuations. This correlation is usually decomposed into so-called slow and rapid contributions arising from turbulence-turbulence and turbulence-mean-flow interactions, respectively. Frequently, so-called wall-reflection corrections are added in order to obtain reasonable predictions near walls. For the LRR RSM these are given in component notation as

$$\begin{aligned} \phi_{ij} &= \phi_{ij,1} + \phi_{ij,2} + \phi_{ij,1}^w + \phi_{ij,2}^w, \\ \phi_{ij,1} &= -C_1 \frac{\epsilon}{k} \left(R_{ij} - \frac{1}{3} \text{tr}(\mathbf{R}) \delta_{ij} \right) = -2C_1 \epsilon (A_{ij}), \\ \phi_{ij,2} &= -C_2 \left(P_{ij} - \frac{1}{3} \text{tr}(\mathbf{P}) \delta_{ij} \right), \\ \phi_{ij,1}^w &= -C_1^w \frac{\epsilon}{k} \left(R_{km} \hat{n}_k \hat{n}_m \delta_{ij} - \frac{3}{2} R_{ki} \hat{n}_k \hat{n}_j - \frac{3}{2} R_{kj} \hat{n}_k \hat{n}_i \right) f\left(\frac{\ell}{y}\right), \\ \phi_{ij,2}^w &= -C_2^w \left(\phi_{km,2} \hat{n}_k \hat{n}_m \delta_{ij} - \frac{3}{2} \phi_{ik,2} \hat{n}_k \hat{n}_j - \frac{3}{2} \phi_{jk,2} \hat{n}_k \hat{n}_i \right) f\left(\frac{\ell}{y}\right). \end{aligned} \quad (26)$$

The slow part $\phi_{ij,1}$ is described by the linear return to isotropy model originally due to Rotta (1951). For the rapid part $\phi_{ij,2}$ the so-called linear isotropization of production model is adopted. This was considered as a simplified version in the work of Launder et al. (1975). Launder (1996) in a discussion of more elaborate variants refers to this combination as the “basic model” while Launder (1991) states that surprisingly often it gives better results than more complex models. The values for the coefficients given in Table 2 below are as recommended in Launder (1996).

In the vicinity of a wall, the velocity fluctuations normal to this wall are damped due to reflection of pressure fluctuations and hence the transfer of energy from the stream-wise to the wall-normal stress component is obstructed. This effect is modeled via the wall-reflection corrections $\phi_{ij,1}^w$ and $\phi_{ij,1}^w$ in Eq. (26) above. Their form was suggested by Gibson and Launder (1978), where \hat{n}_i are the components of the unit vector normal to the wall, and the function f describes the dependence of the corrections on the wall normal distance y scaled by a turbulence length scale ℓ . Taking the mixing length for the latter, i.e. $\ell = C_\mu^{3/4} k^{3/2} \epsilon^{-1}$, and making use of the relation $\ell/y = \kappa$ for the logarithmic sublayer, f is seen to be simply

$$f = \frac{1}{\kappa} \frac{\ell}{y} = \frac{C_\mu^{3/4}}{\kappa y} \frac{k^{2/3}}{\epsilon} . \quad (27)$$

With the values $C_\mu = 0.09$ and $\kappa = 0.41$, the numerical prefactor becomes $C_\mu^{3/4}/\kappa \approx 1/2.5$, which is the form often found in the literature (e.g. Launder 1991).

An alternative model for the pressure-strain correlation has been proposed by Speziale et al. (1991). This model is quadratic in the anisotropy tensor in contrast to the previous relation which is linear in anisotropy. The pressure-strain correlation for the SSG RSM does not introduce extra wall contributions and is given by

$$\begin{aligned} \phi_{ij,1} = & - \left[C_{1a} \epsilon + C_{1b} \frac{1}{2} \text{tr}(\mathbf{P}) \right] A_{ij} \\ & + C_2 \epsilon \left[A_{ik} A_{kj} - \frac{1}{3} A_{mn} A_{mn} \delta_{ij} \right] , \\ \phi_{ij,2} = & \left[C_{3a} - C_{3b} (A_{ij} A_{ij})^{1/2} \right] k D_{ij} \\ & + C_4 k \left[A_{ik} D_{jk} + A_{jk} D_{ik} - \frac{2}{3} A_{mn} D_{mn} \delta_{ij} \right] \\ & + C_5 k (A_{ik} \Omega_{jk} + A_{jk} \Omega_{ik}) . \end{aligned} \quad (28)$$

The values of coefficients given in Table 2 are taken from the original work (Speziale et al. 1991).

For the turbulent dissipation rate ϵ the isotropic assumption is used throughout. Coefficients for the ϵ -equation given in Table 2 have been left at the values proposed by Launder et al. (1975) despite a minor change of $C_{\epsilon 2}$ to 1.83 suggested for the SSG RSM in Speziale et al. (1991).

ϵ -equation RSM	C_ϵ	$C_{\epsilon 1}$	$C_{\epsilon 2}$					
	0.15	1.44	1.92					
R-equation LRR – RSM	C_s	C_1	C_2	C_1^w	C_2^w			
	0.25	1.80	0.60	0.5	0.3			
R-equation SSG - RSM	C_s	C_{1a}	C_{1b}	C_2	C_{3a}	C_{3b}	C_4	C_5
	0.25	3.40	1.80	4.20	0.80	1.30	1.25	0.40

Table 2: Coefficient values for the LRR and SSG RSMs.

2.2.3 Source terms for bubble-induced turbulence

For the source terms added to the turbulence model equations to describe the bubble-induced turbulence (BIT) we first discuss an isotropic version that was previously developed for use with the SST or other two-equation models (Rzehak and Krepper 2013, 2013b). This concerns the source terms S^k and S^ϵ or S^ω in the k - and ϵ - or ω -equations. In a second step we then propose a splitting of the k -source which accounts for the anisotropy of the BIT and is suitable for use with Reynolds stress models. This provides the source term \mathbf{S}^R in the Reynolds stress equation. The source term S^ϵ for the accompanying ϵ -equation remains as for the two-equation models.

The source term S^k in the k -equation describes the additional generation of turbulent kinetic energy due to the presence of the gas bubbles. A plausible approximation for this term is provided by the assumption that all energy lost by the bubble due to drag is converted to turbulent kinetic energy in its wake. This is in accordance with results from the literature (Kataoka et al. 1992, Troshko and Hassan 2001). Hence, the k -source becomes

$$S^k = \mathbf{F}_L^{drag} \cdot (\mathbf{u}_G - \mathbf{u}_L). \quad (29)$$

The source term S_L^ϵ in the ϵ -equation is derived using similar heuristics as for the single-phase model, namely by dividing the k -source by some time scale τ , i.e.

$$S^\epsilon = C_{\epsilon B} \frac{S^k}{\tau}. \quad (30)$$

Further modeling then focusses on the time scale τ , which represents the life-time of a turbulent eddy before it breaks into smaller structures. In a single-phase flow, there are two relevant variables, k and ϵ , and hence only one time scale $\tau = k/\epsilon$ can be formed. For the bubble-induced turbulence in two-phase flows the situation is more complex and several plausible expressions for the time scale are conceivable. The choice $\tau = d_B/\sqrt{k}$ has been shown to give good results (Rzehak and Krepper 2013, 2013a) together with a value of $C_{\epsilon B} = 1.0$.

For the SST or other ω -based models, the ϵ -source term is transformed to an equivalent ω -source term as

$$S^\omega = \frac{1}{C_\mu k} S^\epsilon - \frac{\omega}{k} S^k. \quad (31)$$

Since the ω -source term should be effective throughout the domain, it is employed independently of the blending functions F_1 and F_2 of the SST model.

For the source term \mathbf{S}^R in the Reynolds stress equation we take into account that fluctuations along the direction of bubble motion relative to the liquid and perpendicular to it can be expected to be different. In fact, a recent experiment (Hosokawa and Tomiyama 2013) showed precisely this effect. To express this decomposition mathematically, we make the ansatz

$$\mathbf{S}^R = S^k (a[\hat{\mathbf{u}}_{rel} \otimes \hat{\mathbf{u}}_{rel}] + b[\mathbf{I} - \hat{\mathbf{u}}_{rel} \otimes \hat{\mathbf{u}}_{rel}]), \quad (32)$$

where $\hat{\mathbf{u}}_{rel}$ is a unit vector in the direction of the relative velocity between the bubbles and the liquid, i.e.

$$\hat{\mathbf{u}}_{rel} = \frac{\mathbf{u}_G - \mathbf{u}_L}{|\mathbf{u}_G - \mathbf{u}_L|}. \quad (33)$$

The coefficients a and b , respectively, give the magnitude of fluctuations in the direction of the relative velocity and perpendicular to it. The projection operators $\hat{\mathbf{u}}_{rel} \otimes \hat{\mathbf{u}}_{rel}$ and $\mathbf{I} - \hat{\mathbf{u}}_{rel} \otimes \hat{\mathbf{u}}_{rel}$ projecting on subspaces parallel and perpendicular to the direction of the relative velocity are best visualized by writing the corresponding matrices in a coordinate system with the x-axis aligned with $\hat{\mathbf{u}}_{rel}$ as shown in Figure 1. In this coordinate system,

$$\begin{aligned} \hat{\mathbf{u}}_{rel} \otimes \hat{\mathbf{u}}_{rel} &= \hat{\mathbf{x}} \otimes \hat{\mathbf{x}} = \begin{bmatrix} 1 & 0 & 0 \\ 0 & 0 & 0 \\ 0 & 0 & 0 \end{bmatrix} \\ [\mathbf{I} - \hat{\mathbf{u}}_{rel} \otimes \hat{\mathbf{u}}_{rel}] &= [\mathbf{I} - \hat{\mathbf{x}} \otimes \hat{\mathbf{x}}] = \begin{bmatrix} 0 & 0 & 0 \\ 0 & 1 & 0 \\ 0 & 0 & 1 \end{bmatrix}. \end{aligned} \quad (34)$$

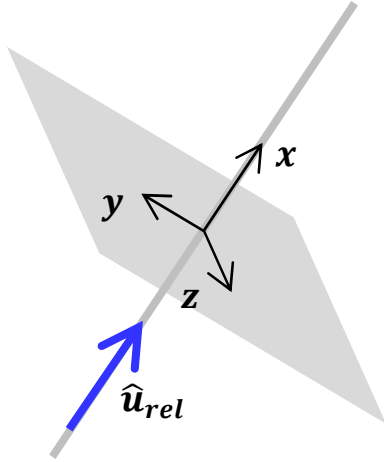


Figure 1: Illustration of projections on the subspaces parallel and perpendicular to $\hat{\mathbf{u}}_{rel}$. In the coordinate system shown, the former subspace is the x-axis and the latter is the yz-plane.

For simple vertical bubble column or pipe flows, such as in the experiments of Hosokawa and Tomiyama (2013) or the simulations of Colombo and Fairweather (2015), $\hat{\mathbf{x}}$ also corresponds with the vertical direction. However, for flows arising in other important applications such as static mixers (Zidouni et al. 2015) or stirred tanks (Shi and Rzehak 2017) no such simple correspondence is valid. To cover these cases as well, the more general coordinate-free expression Eq. (32) has been introduced.

It remains to define values for the coefficients a and b . One relation between the two derives from the requirement that the BIT should contribute the same energy as defined by the k-source S^k above, i.e. $tr(\mathbf{S}^R) = 2S^k$. This requirement yields $a + 2b = 2$. A second relation defines the degree of anisotropy. The experiments of Hosokawa and Tomiyama (2013), which were performed under conditions where the BIT dominates, show that fluctuations along the relative motion are twice as strong as fluctuations perpendicular to the relative motion. This is expressed as $a = 2b$. For comparison, we also consider an isotropic BIT source term with the RSMs, for which obviously $a = b$. The values resulting for a and b are summarized in Table 3.

isotropic \mathbf{S}^R	$a = 2/3$	$b = 2/3$
anisotropic \mathbf{S}^R	$a = 1$	$b = 1/2$

Table 3: Values of a and b for isotropic and anisotropic forms of the BIT source term \mathbf{S}^R in Eq. (32).

2.2.4 Turbulent Wall Function

To avoid the need to resolve the viscous sub-layer, a single-phase turbulent wall function assuming a smooth wall is applied. Depending on whether the turbulence model employs ϵ or ω as independent variable two somewhat different approaches are commonly used (e.g. ANSYS 2012). For ω -based models, analytical solutions are available for both the inertial and the viscous sub-layer (Wilcox 2006, section 4.6.3). Therefore, a wall-function which consists of a blend between inertial and viscous sub-layers can be devised[‡]. For ϵ -based models a simple cut-off is applied to the wall-distance[§]. In both approaches, there is no required minimum size of the first cell near the wall.

The wall-function approach (e.g. Bredberg, 2000) provides an expression for the wall shear stress

$$\tau_W = \rho u_\tau u_k, \quad (35)$$

which gives the flux of momentum into this cell from the wall. This can also be expressed in terms of a modified turbulent viscosity

$$\mu^{turb} = \frac{\tau_W}{|\nabla \mathbf{u}|} - \mu^{mol}, \quad (36)$$

where $\nabla \mathbf{u}$ is evaluated at the face of the first grid cell opposite to the wall.

The compound velocity scales u_τ and u_k are computed as

$$\begin{aligned} u_\tau &= \left[(u_\tau^{viscous})^4 + (u_\tau^{inertial})^4 \right]^{1/4}, \\ u_k &= \left[(u_k^{viscous})^4 + (u_k^{inertial})^4 \right]^{1/4}, \end{aligned} \quad (37)$$

with $u_\tau^{viscous}$, $u_\tau^{inertial}$ and $u_k^{inertial}$ defined as

$$\begin{aligned} u_\tau^{viscous} &= \sqrt{\frac{\mu^{mol} |u|}{\rho y}}, & u_\tau^{inertial} &= \frac{\kappa |u|}{\ln(Ey^*)}, \\ u_k^{inertial} &= C_\mu^{1/4} k^{1/2}, & y^* &= \frac{\rho u_k^{inertial}}{\mu^{mol}} y. \end{aligned} \quad (38)$$

[‡] This approach is termed “automatic near-wall treatment” in the ANSYS CFX User Guide. No reference is quoted there and only partial accounts could be found in the literature (e.g. Vieser et al. 2002, Esch et al. 2003).

[§] This approach is termed “scalable wall function” in the ANSYS CFX User Guide. Again no reference is quoted there.

The alternative velocity scale $u_k^{inertial}$ is introduced to avoid divergence of the viscous length scale when boundary layer separation occurs (Launder and Spalding 1974).

In the above, for y the position of the center of the first grid cell near the wall has to be used while u and k are evaluated at this position. Values of the constants are $\kappa = 0.41$, $C_\mu = 0.09$, and for a smooth wall $E \approx 9.8$. For details on the above formulation refer to Rzehak and Kriebitzsch (2015).

For the turbulent kinetic energy k and the Reynolds stress components R_{ij} a vanishing normal derivative at the wall is applied as a boundary condition.

For the turbulent frequency ω a value is prescribed in the first cell near the wall according to

$$\omega = \left[(\omega^{viscous})^2 + (\omega^{inertial})^2 \right]^{1/2}, \quad (39)$$

where the viscous and log-layer turbulent frequency are given as

$$\begin{aligned} \omega^{viscous} &= \frac{6\mu}{C_{\omega D1} \rho y^2}, \\ \omega^{inertial} &= \frac{u_k^{inertial}}{C_\mu^{1/2} \kappa y} = \frac{k^{1/2}}{C_\mu^{1/4} \kappa y}. \end{aligned} \quad (40)$$

As before, for y the position of the center of the first grid cell near the wall has to be used. $C_{\omega D1} = 0.075$ and all other constants have values as given above.

For the turbulent dissipation rate, a solution is available only for the log-layer but not for the viscous sublayer. Therefore, the approach is taken to limit the y^* value used in the logarithmic law from below as $\tilde{y}^* = \max(y^*, 11.06)$, where $y^* = 11.06$ is approximately the value of y^* at the intersection between the linear viscous and the logarithmic profiles for u . Although this is a crude approach, it avoids catastrophic failure of the standard ϵ wall-function for a fine mesh near the walls. Widespread use of this method, for instance in the work of Masood et al. (2014), justifies its use for the present application. The turbulent dissipation rate at the wall is therefore calculated as

$$\epsilon = \frac{u_k^{inertial}}{\kappa \tilde{y}} = \frac{C_\mu^{3/4} k^{3/2}}{\kappa \tilde{y}} \quad (41)$$

with

$$\tilde{y} = \frac{v_L}{u_k^{inertial}} \tilde{y}^*. \quad (42)$$

Consistently, the calculation of the wall shear stress is based on the log-layer velocity profile only, i.e. $u_k = u_k^{inertial}$, $u_\tau = u_\tau^{inertial}$ replaces Eq. (37) above, and the same limiting procedure is applied to y^* there.

2.3 Interfacial forces

The interfacial force on the gas bubbles \mathbf{F}_G^{inter} (see section 2.1), comprises of the drag and the non-drag forces. The latter in turn include the (shear-) lift force, the wall (-lift) force, the turbulent dispersion force and the virtual mass force, i.e.

$$\mathbf{F}_G^{inter} = \mathbf{F}^{drag} + \mathbf{F}^{lift} + \mathbf{F}^{wall} + \mathbf{F}^{disp} + \mathbf{F}^{VM}. \quad (43)$$

The correlations used for these forces are expressed in terms of three dimensionless numbers, namely the Reynolds (Re), Eötvös (Eo) and Morton (Mo) numbers, defined as

$$\begin{aligned} Re &= \frac{\rho_L |\mathbf{u}_G - \mathbf{u}_L| d_B}{\mu_L}, \\ Eo &= \frac{(\rho_L - \rho_G) g d_B^2}{\sigma}, \\ Mo &= \frac{(\rho_L - \rho_G) g \mu_L^4}{\rho_L^2 \sigma^3}. \end{aligned} \quad (44)$$

For the present purpose, Re can be thought of as non-dimensional relative velocity, Eo as nondimensional bubble size and Mo as dimensionless combination of material properties.

Since detailed discussions are available in the previous works referenced in the introduction, only a brief summary of the pertinent equations is given here to make the model description self-contained.

The gas-phase momentum source for the drag force is given by:

$$\mathbf{F}^{drag} = -\frac{3}{4d_B} C_D \rho_L \alpha_G |\mathbf{u}_G - \mathbf{u}_L| (\mathbf{u}_G - \mathbf{u}_L). \quad (45)$$

A correlation for the drag coefficient distinguishing different shape regimes of the bubbles (spherical, ellipsoidal or cap), was suggested by Ishii and Zuber (1979), namely

$$C_D = \max(C_{D,sphere}, \min(C_{D,ellipse}, C_{D,cap})), \quad (46)$$

where

$$\begin{aligned} C_{D,sphere} &= \frac{24}{Re} (1 + 0.1 Re^{0.75}) \\ C_{D,ellipse} &= \frac{2}{3} \sqrt{Eo} \\ C_{D,cap} &= \frac{8}{3} \end{aligned} \quad (47)$$

This correlation was compared with an extensive data set on the terminal velocity of bubbles rising in quiescent liquids covering several orders of magnitude for each of Re , Eo , and Mo in Tomiyama et al. (1998) with good agreement except at high values of Eo .

The momentum source corresponding to the shear lift force, often simply referred to as lift force, can be calculated as (Zun 1980):

$$\mathbf{F}^{lift} = -C_L \rho_L \alpha_G (\mathbf{u}_G - \mathbf{u}_L) \times \text{rot}(\mathbf{u}_L). \quad (48)$$

For a spherical bubble the shear lift coefficient C_L is positive so that the lift force acts in the direction of decreasing liquid velocity, i.e. in case of co-current pipe flow in the direction towards the pipe wall. If a substantial deformation of the bubble occurs, however, the direction of the lift force changes its sign. From the observation of the trajectories of single air bubbles rising in simple shear flow of a glycerol water solution, the following correlation for the lift coefficient was derived (Tomiyama et al. 2002):

$$C_L = \begin{cases} \min[0.288 \tanh(0.121 Re), f(Eo_{\perp})] & Eo_{\perp} < 4 \\ f(Eo_{\perp}) & 4 < Eo_{\perp} < 10 \\ -0.27 & 10 < Eo_{\perp} \end{cases} \quad (49)$$

with $f(Eo_{\perp}) = 0.00105 Eo_{\perp}^3 - 0.0159 Eo_{\perp}^2 - 0.0204 Eo_{\perp} + 0.474$.

This coefficient depends on the modified Eötvös number defined as

$$Eo_{\perp} = \frac{g(\rho_L - \rho_G)d_{\perp}^2}{\sigma}, \quad (50)$$

where d_{\perp} is the maximum horizontal dimension of the bubble. It is calculated using an empirical correlation for the aspect ratio by Wellek et al. (1966),

$$d_{\perp} = d_B \sqrt[3]{1 + 0.163 Eo^{0.757}}, \quad (51)$$

where Eo is the usual Eötvös number.

Although the Morton number in the experiments on which Eq. (49) is based is lower than for the water-air system at normal conditions, good results have nevertheless been reported for this case (Lucas and Tomiyama 2011).

The general form of the wall lift force, often simply referred to as wall force, is

$$\mathbf{F}^{wall} = \frac{2}{d_B} C_W \rho_L \alpha_G |\mathbf{u}_G - \mathbf{u}_L| \hat{\mathbf{n}}, \quad (52)$$

where $\hat{\mathbf{n}}$ is the unit normal perpendicular to the wall pointing into the fluid. The dimensionless wall force coefficient C_W depends on the distance to the wall y and is expected to be positive so the bubble is driven away from the wall.

Based on the observation of single bubble trajectories in simple shear flow of a glycerol water solution Tomiyama et al. (1995) and later Hosokawa et al. (2002) concluded a functional dependence

$$C_W(y) = f(Eo) \left(\frac{d_B}{2y} \right)^2. \quad (53)$$

In the limit of small Morton number the correlation

$$f(Eo) = 0.0217 Eo \quad (54)$$

can be derived from the data of Hosokawa et al. (2002). As for the shear-lift force, the experiments on which Eq. (54) is based, have a lower Morton number than the water-air system, but good predictions have been obtained also for air bubbles in water (Rzehak and Krepper 2012).

An explicit expression for the turbulent dispersion force was derived in Burns et al. (2004) by Favre averaging the drag force:

$$\mathbf{F}^{disp} = -\frac{3}{4} C_{TD} \frac{\alpha_G}{d_B} |\mathbf{u}_G - \mathbf{u}_L| \frac{\mu_L^{turb}}{\sigma_{TD}} \left(\frac{1}{\alpha_L} + \frac{1}{\alpha_G} \right) \nabla \alpha_G. \quad (55)$$

In analogy to molecular diffusion, σ_{TD} is referred to as a Schmidt number and a value of $\sigma_{TD} = 0.9$ is typically used.

The virtual mass force can be expressed as

$$\mathbf{F}^{VM} = -C_{VM}\rho_L\alpha_G\left(\frac{D_G\mathbf{u}_G}{Dt} - \frac{D_L\mathbf{u}_L}{Dt}\right), \quad (56)$$

where D_G/Dt and D_L/Dt denote material derivatives with respect to the velocity of the indicated phase. For the virtual mass coefficient a value of $C_{VM} = 0.5$ is appropriate (Magnaudet et al. 1995).

3 SUMMARY OF EXPERIMENTAL DATA

To validate the models of section 2, in particular the anisotropic form of the source terms describing the bubble-induced turbulence in conjunction with a Reynolds stress turbulence model, a data base is needed that includes measurements of individual Reynolds stress components in bubbly flows. Only a rather limited number of studies has been published that meet this requirement and are suitable for model validation. The selected test cases comprise three experiments on vertical up-flow of water and air in round pipes with different inner diameters. An overview of the major characteristics of these test cases is given in Table 4. A brief description of each experiment is furnished in the following.

3.1 Tests from Hosokawa et al. (2009, 2010)

The system studied by Hosokawa et al. (2009, 2010) is the vertical up-flow of water and air in a round pipe with inner diameter $D = 25 \text{ mm}$ at atmospheric pressure and room temperature. Radial profiles of the gas fraction, mean liquid and gas velocity, and liquid turbulent kinetic energy were measured at an axial location $L/D = 68$. For some cases, individual components of the Reynolds stresses are also available. In addition, an overall distribution of bubble sizes has been recorded with equivalent spherical diameters determined from a reconstruction of stereoscopic images. The major characteristics of the test cases are shown in Table 4 denoted by the letter 'H'. There, the average values for the gas fraction are obtained from radial averaging of the profiles while the average values of bubble size are obtained from the measured distributions. The experimental data contains both wall and core peaking gas fraction profiles. In addition, turbulence suppression is found for the cases with high liquid velocity, but there is no corresponding trend with regard to bubble size.

3.2 Tests from Liu (1998)

Liu (1998) conducted a study in a vertical up-flow of water and air in a round pipe with inner diameter $D = 57.2 \text{ mm}$ at a temperature of 26°C and presumably atmospheric pressure. Radial profiles of gas fraction, average bubble size, mean axial liquid velocity and axial liquid turbulence intensity were measured at an axial position $L/D = 60$. The average bubble size was computed from measurements of the chord length using a dual needle resistivity probe under the assumption of a spherical bubble shape. The major characteristics of these test cases are shown in Table 4 denoted by the letter 'L'. The average values for both gas fraction and bubble diameter given there are obtained from radial averaging of the measured profiles. All gas fraction profiles possess a wall peak but for the largest bubble size a secondary core peak is also observed. Turbulence suppression occurs in the pipe center for combinations of high liquid and low gas mass flux, which correspond to the smallest bubble sizes.

name	D	$J_{L,nom}$	$J_{G,nom}$	$\langle \alpha_G \rangle$	$\langle d_B \rangle$	$J_{L,adj}$	$J_{G,adj}$
	(mm)	(m/s)	(m/s)	(%)	(mm)	(m/s)	(m/s)
H10	25.0	0.5	-	-	-	-	-
H11	25.0	0.5	0.018	2.5	3.21	0.48	-
H12	25.0	0.5	0.025	4.1	4.25	0.48	0.031
H20	25.0	1.0	-	-	-	-	-
H21	25.0	1.0	0.020	2.8	3.52	0.93	0.035
H22	25.0	1.0	0.036	3.2	3.66	0.96	0.042
L10	57.2	0.5	-	-	-	-	-
L11A	57.2	0.5	0.1	15.2	2.94	-	0.12
L20	57.2	1.0	-	-	-	-	-
L21B	57.2	1.0	0.1	10.6	3.03	-	0.14
L21C	57.2	1.0	0.1	9.6	4.22	-	0.13
L22A	57.2	1.0	0.2	15.7	3.89	-	0.22
S20	200	0.45	-	-	-	-	-
S21	200	0.45	0.015	2.4	4.1	0.41	0.019
S23	200	0.45	0.100	10.7	5.0	0.5	0.108
S30	200	0.68	-	-	-	-	-
S31	200	0.68	0.015	1.7	3.2	0.67	0.018
S33	200	0.68	0.100	10.1	4.7	0.71	0.120

Table 4: Overview of the major characteristics of the selected test cases, where the letter ‘H’ denotes the experimental data provided by Hosokawa et al. (2009, 2010), ‘L’ the cases of Liu (1998), and ‘S’ refers to the data of Shawkat et al. (2008). Nominal values are as reported in the quoted references and adjusted values are obtained as described in section 4.

3.3 Tests from Shawkat et al. (2008)

Shawkat et al. (2008) performed a study in vertical up-flow of water and air in a round pipe with inner diameter $D = 200 \text{ mm}$ at a temperature of $24.5 \text{ }^\circ\text{C}$ and atmospheric pressure. Radial profiles of the gas fraction, average bubble size, mean liquid and gas velocities, and axial as well as radial liquid turbulence intensity and Reynolds shear stress were measured

at an axial position $L/D = 42$. The average bubble diameter was computed as in Liu (1998), but an optical dual needle probe was used instead. The relevant parameters for the selected cases are denoted by the letter 'S' in Table 4. The average values for both gas fraction and bubble diameter given there are obtained from radial averaging of the profiles. A change in the gas fraction profile from wall to core peak with increasing bubble size can be observed. Turbulence suppression at the pipe wall occurs for combinations of high liquid and low gas mass flux, which correspond to the smallest bubble sizes.

4 SIMULATION RESULTS

All models described in section 2 were implemented in OpenFoam v2.4 which was used to run the simulations. Comparison is made between the Reynolds stress models (RSMs) of Launder et al. (1975) (LRR) and of Speziale et al. (1991) (SSG) as well as the two-equation SST model (Menter 2009) for all three sets of test cases described in section 3. For the tests of Hosokawa et al. (2009, 2010), which provide the most detailed measurements of individual Reynolds stress components, in addition, isotropic and anisotropic forms of the BIT source terms are compared. For the tests of Liu (1998) and Shawkat et al. (2008), only the anisotropic BIT is considered to limit the number of simulations runs. The capability of the models to reproduce the measurements of liquid velocity, gas fraction, and turbulent kinetic energy or Reynolds stresses is evaluated.

Like in previous CFD studies of the selected experiments (Rzehak and Krepper 2013b, Kriebitzsch and Rzehak 2016), simulations are performed in a quasi-2D cylindrical geometry, i.e. a narrow cylindrical sector with symmetry boundary conditions imposed on the side faces. The computational domain is extended by 10 to 20% beyond the measurement location to exclude effects from the outlet boundary. A sketch of the simulation geometry is shown in Figure 2. Suitable discretizations have been determined by grid sensitivity studies for the single-phase flow cases of each experiment and both the SST model and the LRR RSM. The necessary numbers of grid points in radial and axial direction, N_x and N_r , are shown in Table 5.

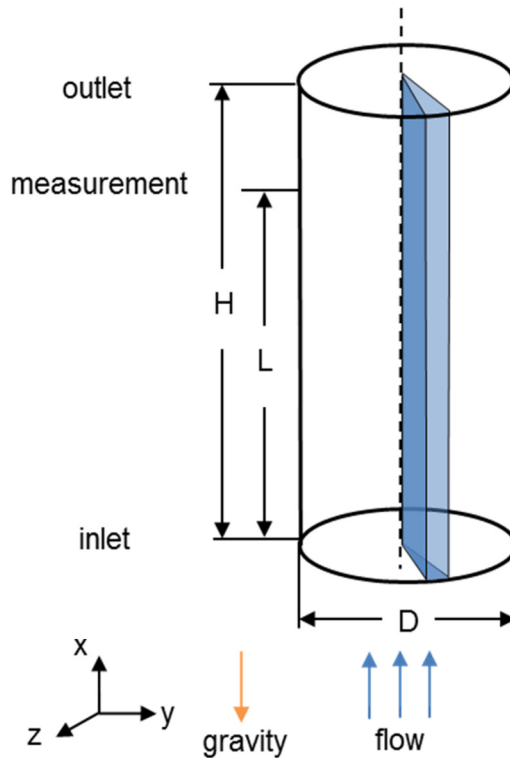


Figure 2: Sketch of the geometry for all test cases. A narrow cylindrical sector of the pipe is considered in the simulations.

On the pipe wall a no-slip condition is used for the liquid phase and a free-slip condition for the gas phase, assuming that direct contacts between the bubbles and the walls are negligible. To avoid the need to resolve the viscous sublayer, the wall functions described in section 2.2.4 are applied. At the bottom, the profile for the liquid velocity is set according to a typical single-phase turbulent flow profile in a pipe as an inlet condition. A turbulent intensity of 5% and a turbulent length scale of $0.1 D$ are used to calculate values of turbulent kinetic energy k_L , frequency ω_L , and dissipation rate ϵ_L at the inlet. The Reynolds stresses at the inlet are assumed to be isotropic and are computed from the turbulent kinetic energy. Gas volume fraction and mass flux are set to uniform values at the inlet. Precise conditions at the inlet do not matter as long as the axial distance to the measurement location is large enough for fully developed conditions to be attained. At the top, a constant pressure is prescribed as an outlet condition while the normal derivatives of the tangential velocity components of both the phases are set to zero. Note that this still permits the normal derivatives of the normal components of both the phases to adjust in the simulation. A vanishing normal derivative is prescribed for other variables.

name	D (mm)	H (m)	L (m)	N_x (-)	N_r (-)
H1*	25	2	1.7	16	400
H2*	25	2	1.7	25	400
L1*	57.2	3.8	3.432	30	650
L2*	57.2	3.8	3.432	57	650
S2*	200	9.24	8.4	100	450
S3*	200	9.24	8.4	100	450

Table 5: Characteristics of the grids used for the simulations of the different test cases. The letter * stands for any number/character matching the names of the test cases in Table 4.

For the tests considered in this work, the bubble size is smaller than 5 mm. In this case, a monodisperse approximation is appropriate. It is therefore applied herein in accordance with the previous works (Rzehak and Krepper 2013b, Kriebitzsch and Rzehak 2016). The average measured bubble diameters are taken as the equivalent spherical diameter of the bubbles in the simulations. Values are given in Table 4 of section 3.

ρ_L	997.0 kg m^{-3}	ρ_G	1.185 kg m^{-3}	σ	0.072 N m^{-1}
μ_L	$8.899\text{e-}4 \text{ kg m}^{-1}\text{s}^{-1}$	μ_G	$1.831\text{e-}5 \text{ kg m}^{-1}\text{s}^{-1}$		

Table 6: Material properties for the air-water system at 25°C temperature and atmospheric pressure.

Both liquid and gas are treated as incompressible fluids with constant material properties. Values of these properties at 25°C temperature and atmospheric pressure are used as summarized in Table 6. Decreasing or increasing the temperature by five degrees results only in minor changes.

While this treatment is computationally advantageous, it introduces some deviation in regard to experimental conditions where the bubbles expand a bit while rising through the pipe due to the pressure drop. As discussed by Rzehak and Krepper (2013) this deviation can be corrected by computing the gas volume flux from the experimental data at the measurement location as^{**}

$$J_G = \frac{2}{R^2} \int_0^{D/2} \alpha_G(r) u_G(r) r dr . \quad (59)$$

In case only the liquid velocity u_L has been measured, the gas velocity u_G can be computed from the liquid velocity based on the fully-developed stationary flow assumption. In some cases, deviations between adjusted values calculated in this way and reported nominal values were also found for the liquid volume flux, which points to some error in the measurements. In these cases, the adjusted values are also used for J_L . Values are again given in Table 4 of section 3.

4.1 Tests of Hosokawa et al. (2009, 2010)

Radial profiles for the liquid velocity obtained from the simulations are plotted in the left column of Figure 3 along with the experimental data for all four test cases. A reasonable agreement is observed for all cases. Somewhat flatter profiles are obtained from the simulations, particularly for the higher liquid volume flux of $J_L = 1.0$ m/s (cases H21, H22), which results in a lower velocity in the pipe centre and a steeper decrease near the wall. Only subtle differences can be noticed between the profiles for SST, LRR and SSG models, where the last tends to be the flattest in the pipe center and the steepest near the wall while the first shows the opposite trend. There is no difference between the isotropic and anisotropic BIT models.

The middle column of Figure 3 shows the calculated and measured gas fraction profiles for all four test cases. Pronounced wall peaks in the experimental gas fraction profiles are observed for a liquid superficial velocity of $J_L = 1.0$ m/s (cases H21, H22), while for $J_L = 0.5$ m/s (cases H11, H12) the profiles are rather flat. This difference is captured by the simulations using RSMs, but not by those using the SST model which show a distinct wall peak for all cases. All models overpredict the height of the wall peak for the higher liquid flux, but to a somewhat lesser degree for the RSMs, with the SSG RSM offering a slight advantage over the LRR RSM for case H22. However, for case H12, which has notably larger bubbles than all other test cases (~ 4 mm rather than $\sim 1.5 \dots 3$ mm), the LRR RSM performs much better than the SSG RSM. Between the isotropic and anisotropic BIT models, only a minor difference is realized.

^{**} This formula corrects an erroneous prefactor in Rzehak and Krepper (2013) and Rzehak and Kriebitzsch (2015).

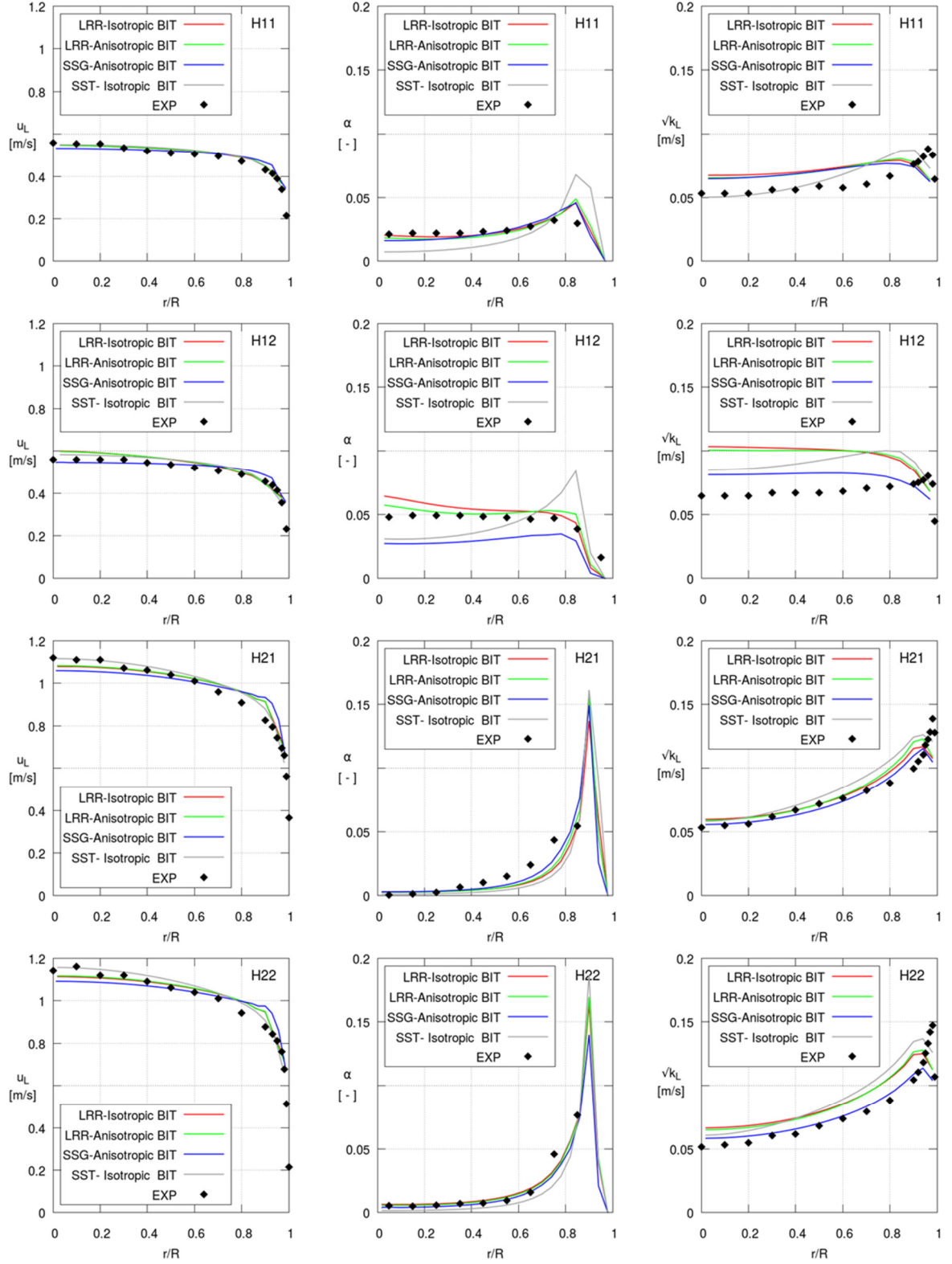


Figure 3: Comparison between simulations and experimental data for the tests from Hosokawa et al. (2009, 2010). The columns give from left to right the radial profiles of the mean liquid velocity, the gas fraction, and the turbulent kinetic energy. Each row contains results for one test case as noted on the graphs. Different models for the liquid turbulence are considered as indicated in the legend.

For the turbulent kinetic energy shown in the right column of Figure 3, the simulation results match the experimental measurements reasonably well for the cases with higher liquid flux, H21 and H22. For these cases differences between the models are only minor with the SSG RSM providing a slightly better match. For the cases with lower liquid flux, H11 and H12, the SST model gives a more peaked profile shape than the RSMs, but the overall agreement with the data is similar. For the case H11 differences between the RSMs are insignificant, but for case H12 with larger sized bubbles, the SSG model provides a notably better match. For all cases and all models, the peak in k near the wall is not captured very well. For the RSMs this could be related to the lack of advanced wall functions, but the rather similar behavior of the SST model in this respect suggests that this may be a general shortcoming of the RANS approach. Again, there is only a minimal difference between the isotropic and anisotropic BIT models.

Figure 4 and Figure 5 show the individual Reynolds stresses for the cases H11 and H22, for which measurements are available. From the comparison of the isotropic and anisotropic BIT models in Figure 4 it is seen that the anisotropic model comes a bit closer to the data for the lateral normal stresses $\langle v'v' \rangle$ and $\langle w'w' \rangle$ but is correspondingly further away for the axial normal stress $\langle u'u' \rangle$. All the normal stresses are somewhat overpredicted in the pipe center, but the peak in the axial normal stress near the pipe wall is underpredicted. For the shear stress $\langle u'v' \rangle$ both variants for the BIT model exactly agree with each other and with the measured data. Though the improvement by the anisotropic BIT model is less clear than what might have been expected, this model will be used from here on.

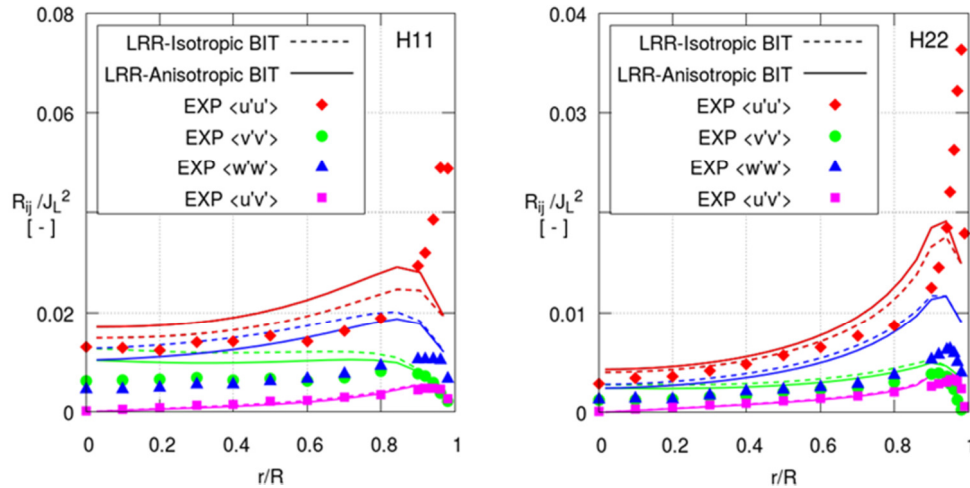


Figure 4: Radial profiles of the Reynolds stress components calculated using different models for the bubble-induced turbulence as indicated in the legend together with the LRR RSM in comparison with the available experimental data from Hosokawa et al. (2009, 2010).

From the comparison of the LRR and SSG RSMs in Figure 5, it is seen that the SSG model produces flatter profiles for the normal stresses which is more in accord with the measured data for the lateral normal stresses. The loss of accuracy for the wall peak in the axial normal stress is insignificant in view of the large deviation from the measured data. For the shear stress both RSMs exactly agree with each other and with the measured data.

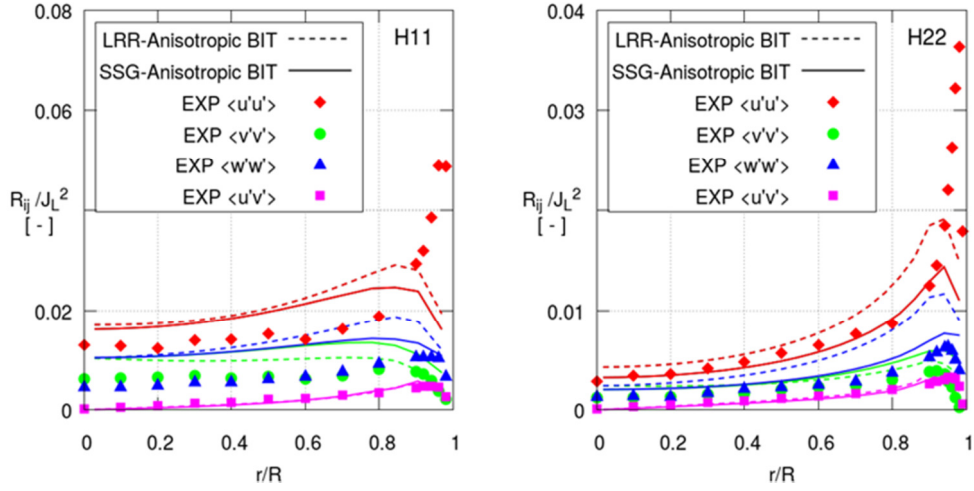


Figure 5: Radial profiles of the Reynolds stress components using different models for the liquid turbulence as indicated in the legend together with the anisotropic source terms for the bubble-induced turbulence in comparison with the available experimental data of Hosokawa et al. (2009, 2010).

Overall, it may be concluded that the SSG model provides a relatively better match with the experiment than the LRR model, the only exception being the gas fraction profile for case H12.

4.2 Tests from Liu (1998)

The investigation is continued to demonstrate the advantage of using RSMs over simple two-equation turbulence models for additional test cases under different conditions, namely a larger pipe diameter. Based on the findings of the previous section, further evidence is sought, which RSM is most suitable, but only the anisotropic BIT model will be used.

The profiles of liquid velocity obtained from the simulations are compared with the measurement data of Liu (1998) in the left column of Figure 6. For the cases L21B and L22A, the measured profiles are flat for most of the pipe radius and decrease only close to the wall, while for the cases L11A and L21C the decrease extends over a large part of the pipe radius. From the flow parameters, no simple trend can be identified for this different behavior. The SSG model captures the profile for cases L21B and L22A very closely, but predicts a profile which is too flat in the center and too steep near the wall for cases L11A and L21C. The profiles for the LRR model are too sloped for the cases L21B and L22A, but still too flat for cases L11A and L21C. The profiles for SST and SSG models almost coincide with each other.

In the center column of Figure 6, the profiles of the gas fraction are shown, all of which show wall-peaks. In the center of the pipe there is a good agreement between all models and the experimental data. Slight deviations are seen for case L21C where an experimentally found second shallow peak in the pipe center is missed by all the models. Noticeable differences are observed near the wall, where the gas fraction peak is overpredicted by all models, but to a strongly different degree. In contrast with the SST model which results in too high peak values for all tests, still reasonable values are obtained for the RSMs with the SSG model providing slightly better results than the LRR model.

In the right column of Figure 6, the computed radial profiles of the axial Reynolds stress are plotted against the measured ones. For the SST model, which provides only a value for the turbulent kinetic energy $k = (\langle u'u' \rangle + \langle v'v' \rangle + \langle w'w' \rangle)/2$, two curves are plotted, one of which corresponds to the limit of unidirectional fluctuations, where $2k = \langle u'u' \rangle$, while the other one assumes isotropic fluctuations with $2k/3 = \langle u'u' \rangle$. Clearly, the former produces significantly too large values, while latter is in reasonable agreement with experimental data. However, since the RSMs, which provide values for $\langle u'u' \rangle$ directly, consistently give higher values, some anisotropy was apparently present. Except for the double-peaked case L21C, values in the pipe center tend to be too high for all models. The wall peak in the profiles tends to be too low for all models, but the RSMs outperform the SST model in this respect, with the LRR model providing slightly better agreement with the measurement than the SSG model.

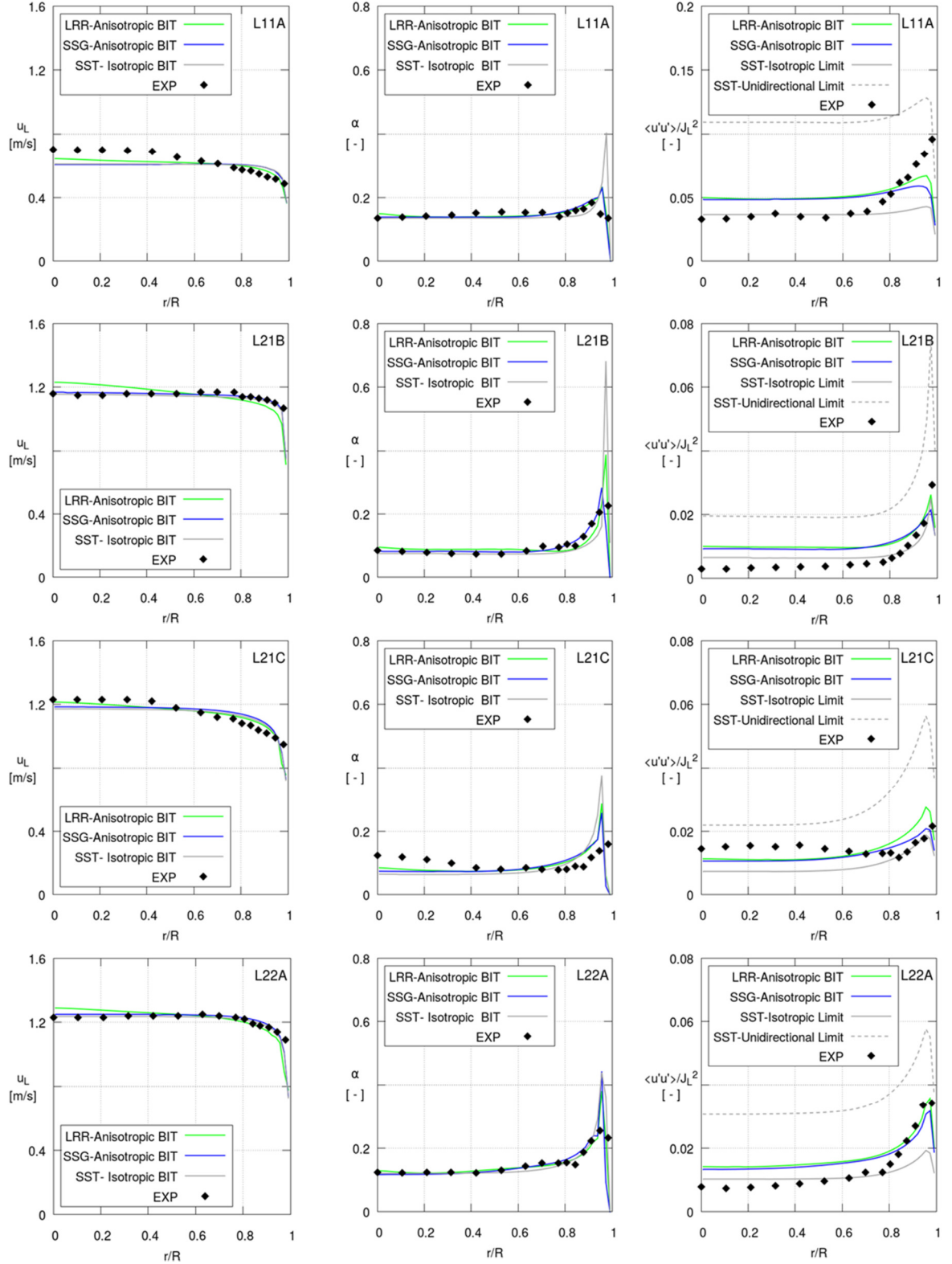


Figure 6: Comparison between simulations and experimental data for the tests from Liu (1998). The columns give from left to right the radial profiles of the mean liquid velocity, the gas fraction and the intensity of axial turbulent fluctuations. Each row contains results for one test case as noted on the graphs. Different models for the liquid turbulence are considered as indicated in the legend.

4.3 Tests from Shawkat et al. (2008)

In the same vein, as in the previous section, the model comparison is further extended to a set of test cases with yet higher pipe diameter.

The profiles of liquid velocity obtained from the simulations are compared with the experimental data of Shawkat et al. (2008) in the left column of Figure 7. For the cases with lower superficial gas velocities (S21, S31) the profiles are flat for most of the pipe and decrease only close to the wall, while for the higher gas flux cases (S23, S33) the decrease occurs more gradually over the whole pipe. For the lower gas flux cases the simulations match very well with the experiments, with the results from all three turbulence models almost coinciding. For the higher gas flux cases, significant deviations are observed. The simulations still produce flat profiles in the pipe core with a steep decrease near the wall, whereas the measurements give profiles showing a decrease of velocity from the center towards the wall over almost the entire pipe radius ($r/R > 0.2$). A possible explanation of this can be related to larger bubbles involved for cases S23 and S33, which due to the lift force (see section 2.3) have a tendency to move towards the pipe center, where they drag the liquid with them during their rise. Since the true (unknown) bubble size distribution in the experiment has a certain width, this effect is only incompletely captured by the monodisperse approximation used herein.

As depicted in the middle column of Figure 7, showing the gas fractions, wall-peaked profiles are obtained in the experiments at lower gas fluxes (S21, S31). For these cases, the gas fraction is well predicted by the simulations in the core region. The height of the wall peak is overestimated by the models with the RSMs mostly performing better than the SST model. No wall peak is visible in the experimental data for the cases S23 and S33, instead the gas fraction increases monotonically towards the pipe center. However, in the simulations, a pronounced wall-peak is still present for all models. Differences between LRR and SSG models are only minor for all test cases.

The right column of Figure 7 shows the comparison of calculated axial Reynolds stresses with the experimental data. As before, for the SST model two curves are plotted, corresponding to the limits of unidirectional and isotropic fluctuations. Comparison with the RSMs suggests that a mild anisotropy is present. For the lower gas flux cases, S21 and S31, these results are also in accordance with the measurements. For the higher gas flux cases, S23 and S33, however, they significantly underpredict the measurements. Again this may be related to the monodisperse approximation as discussed above. For the tests of Shawkat et al. (2008) also the radial Reynolds stresses were measured and these are compared with the simulation results for the LRR and SSG models in Figure 8. Agreement between simulations here is good for the high liquid flux cases, S23 and S33, while deviations are seen for lower liquid flux. Differences between the LRR and SSG models are small for both Reynolds stress components and all cases.

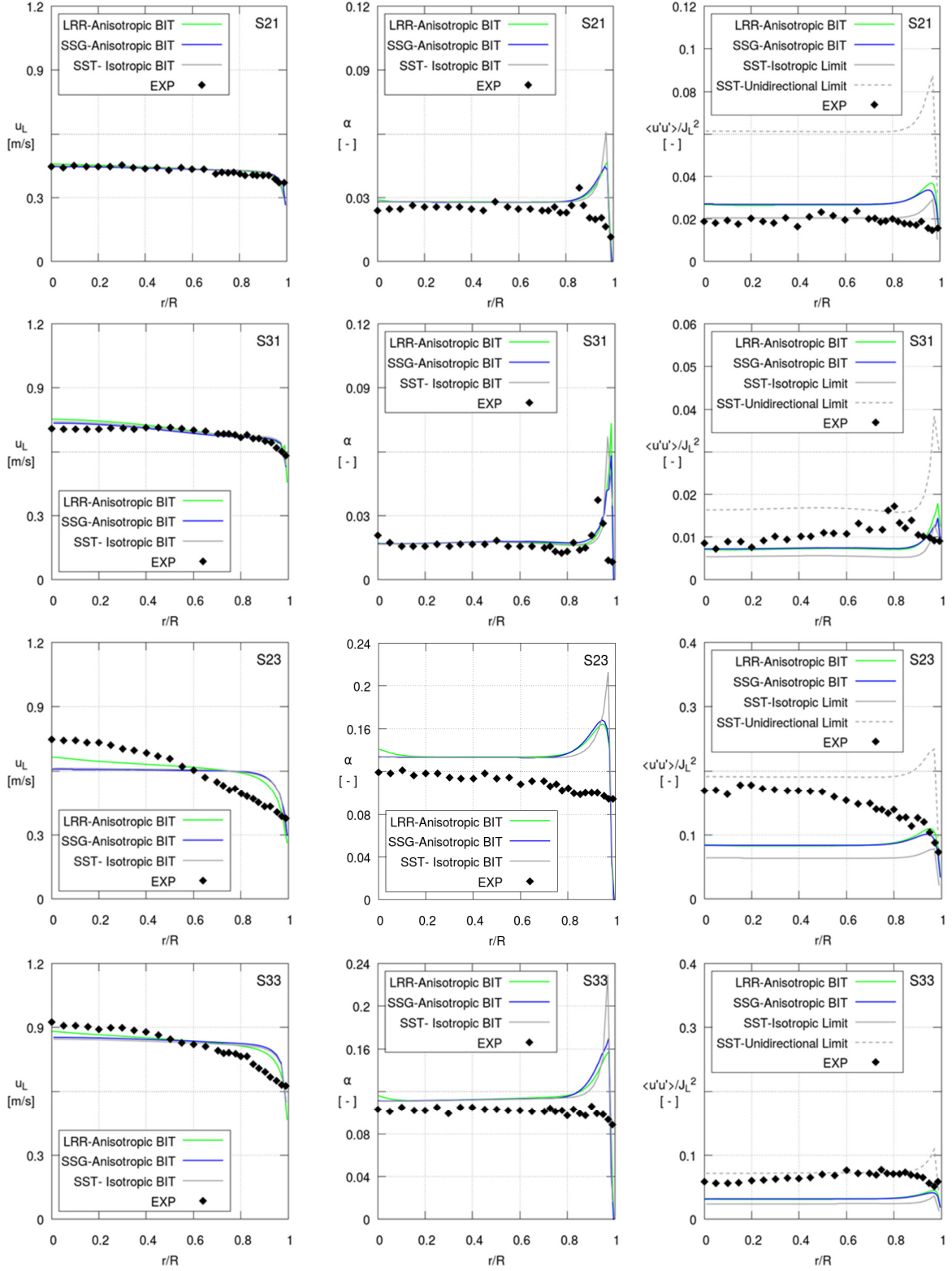


Figure 7: Comparison between simulations and experimental data for the tests from Shawkat et al. (2008). The columns give from left to right the radial profiles of the mean liquid velocity, the gas fraction and the intensity of axial turbulent fluctuations. Each row contains results for one test case as noted on the graphs. Different models for the liquid turbulence are considered as indicated in the legend.

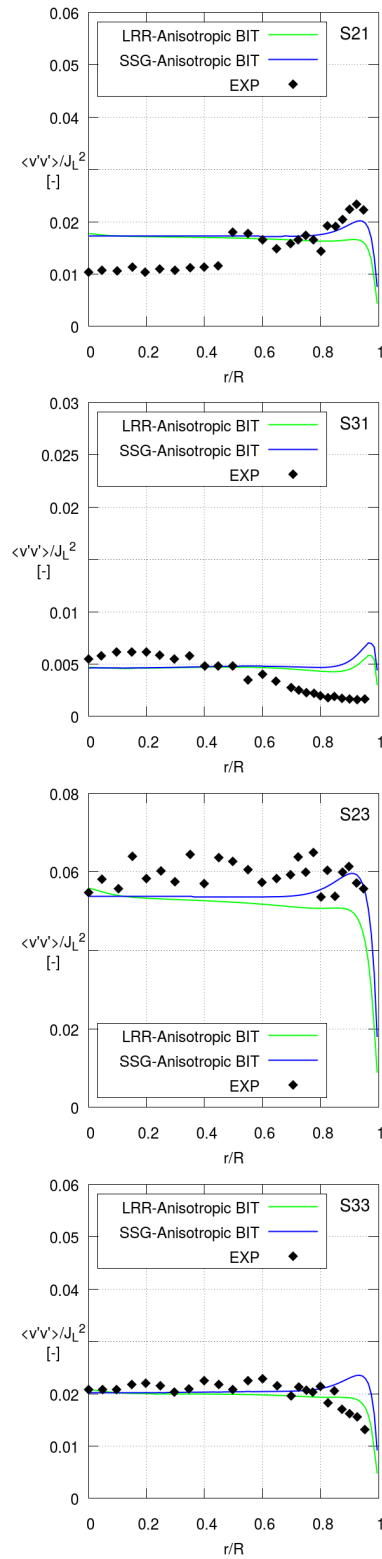


Figure 8: Continued comparison between simulations and experimental data for the tests from Shawkat et al. (2008) giving the radial profiles of radial turbulent fluctuations. Each row contains results for one test case as noted on the graphs. Different models for the liquid turbulence are considered as indicated in the legend.

5 DISCUSSION AND CONCLUSIONS

Bubbly flows were studied by CFD simulations based on the two-fluid Euler-Euler framework using the OpenFOAM code. Special focus of the work was the modeling of turbulence, which has a great impact on other aspects of bubbly flows like coalescence and breakup of the bubbles (Liao et al. 2015, Rzehak et al. 2015) or heat and mass transfer between the bubbles and the liquid (Rzehak 2016, Rzehak and Krepper 2016, Krauß and Rzehak 2017). In contrast to the majority of previous studies in this field, Reynolds stress models were used that capture the anisotropy of turbulent fluctuations and a comparison was made between two common ones, namely those of Launder, Reece and Rodi (LRR, Launder et al. 1975) and Speziale, Sarkar and Gatski (SSG, Speziale et al. 1991). For bubbly flows, in addition to the shear-induced turbulence well-known from single-phase flows, a bubble-induced contribution has to be considered. Corresponding anisotropic source terms for the bubble induced turbulence were developed. By basing the anisotropy on the direction of the relative velocity the physics governing this effect is taken into account, which represents an advantage over an otherwise similar previous formulation (Colombo and Fairweather, 2015), where the anisotropy was based on a fixed coordinate frame. The strength of the anisotropy was defined according to an experiment under conditions where the shear-induced turbulence is low (Hosokawa and Tomiyama 2013). Other aspects of the model, in particular the bubble forces, were taken exactly like in a previously validated baseline model. That baseline model used a two-equation model for the turbulence and comparison with this model was included as a reference.

To validate the model a database of measurements in upwards vertical pipe flows of air bubbles in water was gathered from the literature. The experimental conditions comprise three different pipe diameters and a range of gas and liquid fluxes. Bubble sizes vary between 3 and 5 mm. An important criterion for the selection was that the data should include measurements of the liquid turbulence, preferably with individual Reynolds stresses resolved. In addition, measurements of the mean liquid velocity and the gas fraction were used to compare with the simulation results.

Comparison between simulation results and experimental data for individual Reynolds stresses showed that these can be predicted by both the LRR and SSG Reynolds stress models including the bubble-induced turbulence with an accuracy that is comparable to previous predictions of the turbulent kinetic energy based on the two-equation $k-\omega$ SST model. Since two-equation models by construction cannot resolve the anisotropy of turbulent fluctuations, this represents a significant improvement of the modeling. All models showed a tendency to underpredict the wall peaks in the turbulent kinetic energy and Reynolds stresses seen in the experimental data. This underprediction was found worse for the $k-\omega$ SST model than for the two Reynolds stress models between which no clear trend could be identified. Concerning the bubble-induced turbulence, differences between simulation results obtained with isotropic and anisotropic source terms were not very big. However, this is likely due to the fact that the investigated tests have rather simple mean flows with parallel streamlines. For flows with more complex structure this may be different and hence it is nonetheless recommended to use the anisotropic version for future applications.

Concerning the mean liquid velocity, there were only small differences between all models, but for the gas fraction, a notable improvement was found for the Reynolds stress models.

Common to all models is a tendency to overpredict the gas fraction peaking near the wall. This overprediction was found worse for the $k-\omega$ SST model than for the Reynolds stress models with the LRR model slightly inferior to the SSG model. For cases with core-peaking gas fraction profiles deviations to the experiments were most pronounced. None of the models reproduced the core peak in the gas fraction and the related gradual variation of the liquid velocity profiles. This shortcoming is likely to be linked with the assumption of a constant bubble size and improvements can be expected by employing multi-group population balance methods. However, experimental data providing also the measured bubble size distributions, which are then needed either as input to the model or to validate the predictions thereof, are very scarce. To summarize, both Reynolds stress models improved the overall agreement with the measurements with the SSG model providing a somewhat better match than the LRR model.

The enhanced capabilities of Reynolds stress models to describe the turbulence field and its anisotropy can be further exploited for simulating more complex two-phase flows that are affected by the known inadequacies of the two-equation turbulence models such as static mixers (Zidouni et al. 2015) or stirred tanks (Shi and Rzehak 2017). This necessitates the availability of reliable high-quality experimental data for such flows which should include measurements of individual Reynolds stresses. In addition, information on the bubble size distribution is essential to understand bubbly flow phenomena and is indeed a pre-requisite for plausible modeling and simulation of turbulent bubbly flows.

Further desirable improvements of turbulence modeling for two-phase flows include the following. Since the largest deviations are found close to the walls, an ω based formulation or a blend similar to that used in the SST model may be expected to be beneficial also for RSMs (Wilcox 2006 ch 6.3.3, Menter 2012). In addition, a combination of LRR and SSG models in the near-wall and pipe-center regions, respectively, which was proposed recently for single-phase flows (Cecora et al. 2012), could produce improved results in these regions, respectively. The development of truly two-phase wall functions is more challenging and previous attempts within the framework of two-equation turbulence models (Troshko and Hassan 2001a) have not yet lead to a conclusive and generally accepted solution. Still such a development would be highly desirable also when adapted to the framework of Reynolds stress models. Finally, a more precise account for anisotropy may be sought in the bubble-induced turbulence by including non-normal bubble-induced Reynolds stress components.

6 ACKNOWLEDGEMENT

This work has been carried out in the frame of a research project (GZ: RZ 11/1-1) within the DFG Priority Programme 1740: "Reactive Bubbly Flows" funded by the DFG.

7 NOMENCLATURE

Latin Formula Characters*

Symbol	Description	Unit	Symbol	Description	Unit
--------	-------------	------	--------	-------------	------

A	Anisotropy tensor	-	Mo	Morton number	-
C_D	Drag coefficient	-			
C_L	Lift coefficient	-	L	Length of test section	m
C_{TD}	Turbulent dispersion coefficient	-	N_r	Number of cells in radial direction	-
C_{VM}	Virtual mass force coefficient	-	N_z	Number of cells in axial direction	-
C_W	Wall force coefficient	-	\hat{n}	Wall normal unit vector	-
C_μ	Shear-induced turbulence coefficient ($k - \omega$ SST model)	-	p	Pressure (static)	Pa
d_B	Bulk bubble diameter	m	r	Radial coordinate	m
d_\perp	Bubble diameter perpendicular to main motion	m	R	Pipe radius	m
D	Pipe diameter	m	R	Reynolds stress tensor	$\text{m}^2 \text{s}^{-2}$
D	Strain rate tensor	s^{-1}	Re	Reynolds number	-
				Source term due to bubble- induced turbulence	-
E	Constant in wall function	-	S		
Eu	Eötvös number	-	t	Time	s
Eu_\perp	Modified Eötvös number	-	T	Temperature	$^\circ\text{C}$
F_1	First blending function ($k - \omega$ SST model)	-	T	Stress tensor	N m^{-2}
F_2	Second blending function ($k - \omega$ SST model)	-	u	Mean velocity	m s^{-1}
F	Force per unit volume	N m^{-3}	u'	Fluctuating velocity	m s^{-1}
g	Acceleration of gravity	m s^{-2}	u_τ	Friction velocity	m s^{-1}
H	Total height of simulated pipe	m	\hat{u}_{rel}	unit vector in direction of relative velocity	
I_{turb}	Turbulence intensity	-	u^*	Velocity scale in logarithmic region	m s^{-1}
I	Identity tensor	-	x	Axial coordinate	m
J	Superficial velocity = volumetric flux	m s^{-1}	y	Wall normal coordinate	m
k	Specific turbulent kinetic energy	$\text{m}^2 \text{s}^{-2}$	y^*	Dimensionless distance from the wall	-
ℓ	Turbulent length scale	m	z	Spanwise coordinate	m

Greek Formula Characters*

Symbol	Description	Unit	Symbol	Description	Unit
α	Phase fraction	-	τ	Time scale	s

ϵ	Turbulent dissipation rate	$\text{m}^2 \text{s}^{-3}$	τ_w	Wall shear stress	N m^{-2}
κ	Von Karman constant	-	ϕ	Momentum flux	$\text{m}^3 \text{s}^{-1}$
$\mu, \boldsymbol{\mu}$	Dynamic viscosity	$\text{kg m}^{-1} \text{s}^{-1}$	Φ	Pressure-strain term	$\text{m}^2 \text{s}^{-3}$
ν	Kinematic viscosity	$\text{m}^2 \text{s}^{-1}$	χ	Interpolated constant	-
ρ	Density	kg m^{-3}	ω	turbulent frequency	s^{-1}
σ	Surface tension	N m^{-1}	Ω	Rotation rate tensor	s^{-1}

Latin Indices*

Symbol	Description	Symbol	Description
<i>adj</i>	Adjusted values	<i>inertial</i>	In inertial layer
<i>body</i>	On body	<i>L</i>	Liquid phase
<i>cap</i>	Spherical cap form	<i>lift</i>	Due to shear-lift
<i>disp</i>	Due to turbulent dispersion	<i>mix</i>	For mixture
<i>drag</i>	Due to drag/ resistance	<i>mol</i>	Molecular
<i>eff</i>	Effective	<i>nom</i>	Nominal values
<i>ellipse</i>	Ellipsoidal form	<i>sphere</i>	Spherical form
<i>G</i>	Gas phase	<i>turb</i>	Turbulent
<i>k</i>	k^{th} phase	<i>vis</i>	In viscous sublayer
<i>i, j</i>	Cartesian vector / tensor components	<i>wallvis</i>	Due to wall-liftIn viscous sublayer
<i>inter</i>	On interface	<i>wall</i>	Due to wall-lift

* Constants and fit functions appearing only once in specific correlations have been omitted for the sake of clarity.

8 REFERENCES

ANSYS, 2012. ANSYS CFX-Solver Theory Guide Release 14.5. *ANSYS Inc.*

Arnold, G. S., Drew, D. A., and Lahey, R. T. Jr, 1989. Derivation of constitutive equations for interfacial force and Reynolds stress for a suspension of spheres using ensemble cell averaging. *Chemical Engineering Communications* 86, 43–54.

Bredberg, J., 2000. On the wall boundary condition for turbulence models. Technical report, *Chalmers University of Technology*.

Burns, A. D., Frank, T., Hamill, I., Shi, J.-M., 2004. The Favre averaged drag model for turbulence dispersion in Eulerian multi-phase flows. *Proc. 5th Int. Conf. on Multiphase Flow, ICMF2004*, Yokohama, Japan.

Cecora, R.-D., Eisfeld, B., Probst, A., Crippa, S., and Radespiel, R., 2012. Differential Reynolds stress modeling for aeronautics. *50th AIAA Aerospace Sciences Meeting including the New Horizons Forum and Aerospace Exposition*, Nashville, Tennessee, paper AIAA 2012-0465.

- Colombo, M. and Fairweather, M., 2015. Multiphase turbulence in bubbly flows: RANS simulations. *International Journal of Multiphase Flow* 77, 222–243.
- Daly, B. J. and Harlow, F. H., 1970. Transport equations in turbulence. *Physics of Fluids* 13, 2634–2649.
- Drew, D. A., Passman, S. L., 1998. Theory of Multicomponent Fluids, *Springer*.
- Ekambara, K. and Dhotre, M. T., 2010. CFD simulation of bubble column. *Nuclear Engineering and Design* 240, 963–969.
- Esch, T., Menter, F. and Vieser, W., 2003. Heat transfer predictions based on two-equation turbulence models. *Proceedings of the 6th ASME-JSME Thermal Engineering Joint Conference*, paper TED-AJ03-542.
- Gibson, M. M. and Launder, B. E., 1978. Ground effects on pressure fluctuations in the atmospheric boundary layer. *Journal of Fluid Mechanics* 86, 491–511.
- Hosokawa, S., Tomiyama, A., Misaki, S. and Hamada, T., 2002. Lateral migration of single bubbles due to the presence of wall. *Proc. ASME Joint U.S.-European Fluids Engineering Division Conference*, FEDSM2002, Montreal, Canada.
- Hosokawa, S. and Tomiyama, A., 2009. Multi-fluid simulation of turbulent bubbly pipe flows. *Chemical Engineering Science* 64, 5308–5318.
- Hosokawa, S. and Tomiyama, A., 2010. Effects of bubbles on turbulent flows in vertical channels. *7th Int. Conf. Multiph. Flow*, 1–11.
- Hosokawa, S. and Tomiyama, A., 2013. Bubble-induced pseudo turbulence in laminar pipe flows. *International Journal of Heat and Fluid Flow* 40, 97–105.
- Ishii, M. and Hibiki, T., 2011. Thermo-fluid dynamics of two-phase flow. *Springer*, 2nd ed.
- Ishii, M. and Zuber, N., 1979. Drag coefficient and relative velocity in bubbly, droplet or particulate flows. *AIChE Journal* 25, 843–855.
- Kataoka, I., Besnard, D. C., and Serizawa, A. 1992. Basic equation of turbulence and modeling of interfacial transfer terms in gas-liquid two-phase flow. *Chemical Engineering Communications* 118, 221–236.
- Krauß, M. and Rzehak, R., 2017. Reactive absorption of CO₂ in NaOH: Detailed study of enhancement-factor models. *Chemical Engineering Science* 166, 193–209.
- Kriebitzsch, S. and Rzehak, R., 2016. Baseline model for bubbly flows: simulation of monodisperse flow in pipes of different diameters. *Fluids* 1, 29.
- Lahey, R. T. Jr, Lopez de Bertodano, M., and Jones, O. C. J., 1993. Phase distribution in complex geometry conduits. *Nuclear Engineering and Design* 141, 177–201.
- Launder, B.E. and Spalding, D.B., 1974. The numerical computation of turbulent flows. *Computer Methods in Applied Mechanics and Engineering* 3, 269–289.
- Launder, B. E., Reece, G. J. and Rodi W., 1975. Progress in the development of a Reynolds stress turbulence closure. *Journal of Fluid Mechanics* 68, 537–566.
- Launder, B. E., 1991. Current capabilities for modeling turbulence in industrial flows. *Applied Scientific Research* 48, 247-269.

- Launder, B. E., 1996. An introduction to single-point closure methodology. In Gatski, T. B. Hussaini, M. Y., and Lumley, J. L. (Eds.): *Simulation and Modeling of Turbulent Flows*, Oxford University Press, 243–310.
- Lee, S. Lahey, R. T. Jr, and Jones, O., 1989. The prediction of two-phase flow turbulence and phase distribution using a k-epsilon model. *Japanese Journal of Multiphase Flow* 3, 335–368.
- Liao, Y., Rzehak, R., Lucas, D. and Krepper, E., 2015. Baseline closure model for dispersed bubbly flow: Bubble coalescence and breakup. *Chemical Engineering Science* 122, 336–349.
- Liao, J., Ziegenhein, T., and Rzehak, R., 2016. Bubbly flow in an airlift column: a CFD study. *Journal of Chemical Technology & Biotechnology* 91, 2904–2915.
- Liu, T. J., 1998. The role of bubble size on liquid phase turbulent structure in two-phase bubbly flow. *Proc. 3rd Int. Conf. on Multiphase Flow*, ICMF1998, Lyon, France.
- Lopez de Bertodano, M., Lee, S.-J., Lahey, R. T. Jr, and Drew, D. A., 1990. The prediction of two-phase turbulence and phase distribution phenomena using a Reynolds stress model. *Journal of Fluids Engineering* 112, 107–113.
- Lucas, D. and Tomiyama, A., 2011. On the role of the lateral lift force in poly-dispersed bubbly flows. *International Journal of Multiphase Flow* 37, 1178–1190.
- Magnaudet, J., Rivero, M., and Fabre, J., 1995. Accelerated flows past a rigid sphere or a spherical bubble Part 1: Steady straining flow. *Journal of Fluid Mechanics* 284, 97–135.
- Masood, R. M. A., Rauh, C., and A. Delgado, 2014. CFD simulation of bubble column flows: An explicit algebraic Reynolds stress model approach. *International Journal of Multiphase Flow* 66, 11–25.
- Menter, F. R., 2009. Review of the shear-stress transport turbulence model experience from an industrial perspective. *International Journal of Computational Fluid Dynamics* 23, 305–316.
- Menter, F. R., Garbaruk, A. V., and Egorov, Y., 2012. Explicit algebraic Reynolds stress models for anisotropic wall-bounded flows. *Progress in Flight Physics* 3, 89–104.
- Mimouni, S., Archambeau, F., Boucker, M., Lavieville, J., and Morel, C., 2009. A second-order turbulence model based on a Reynolds stress approach for two-phase flow - Part I: Adiabatic cases. *Science and Technology of Nuclear Installations* 2009, 792395
- NASA, 2014. Turbulence Modeling Resource. NASA Langley Research Center, <http://turbmodels.larc.nasa.gov/index.html>.
- OpenCFD, 2015. OpenFOAM User Guide v2.4.0. *OpenFOAM Foundation*.
- Politano, M. S., Carrica, P. M., and Converti, J., 2003. A model for turbulent polydisperse two-phase flow in vertical channels. *International Journal of Multiphase Flow* 29, 1153–1182.
- Riboux, G., Legendre, D., and Risso, F. A., 2013. Model of bubble-induced turbulence based on large-scale wake interactions. *Journal of Fluid Mechanics* 719, 362–387.
- Rodi, W. , 1976. A new algebraic relation for calculating the Reynolds stresses. *Zeitschrift für angewandte Mathematik und Mechanik* 56, T219–T221.
- Rotta, J., 1951. Statistische Theorie nichthomogener Turbulenz. *Zeitschrift für Physik* 129, 547–572 (in German).

- Rzehak, R., Krepper, E., and Lifante, C. , 2012. Comparative study of wall-force models for the simulation of bubbly flows. *Nuclear Engineering and Design* 253, 41–49.
- Rzehak, R. and Krepper, E., 2013. Bubble-induced turbulence: Comparison of CFD models. *Nuclear Engineering and Design* 258, 57–65.
- Rzehak, R. and Krepper, E., 2013a. Closure models for turbulent bubbly flows: a CFD study. *Nuclear Engineering and Design* 265, 701–711.
- Rzehak, R. and Krepper, E., 2013b. CFD modeling of bubble-induced turbulence. *International Journal of Multiphase Flow* 55, 138–155.
- Rzehak, R. and Krepper, E., 2015. Bubbly flows with fixed polydispersity: Validation of a baseline closure model. *Nuclear Engineering and Design* 287, 108–118.
- Rzehak, R. and Kriebitzsch, S., 2015. Multiphase CFD-simulation of bubbly pipe flow: A code comparison. *International Journal of Multiphase Flow* 68, 135–152.
- Rzehak, R., Krepper, E., Liao, Y., Ziegenhein, T., Kriebitzsch, S. and Lucas, D., 2015. Baseline model for the simulation of bubbly flows. *Chemical Engineering and Technology* 38, 1972–1978.
- Rzehak, R., Krepper, E., 2016. Euler-Euler Simulation of Mass-transfer in Bubbly Flows. *Chemical Engineering Science* 155, 459–568.
- Rzehak, R. 2016. Modeling of Mass-transfer in Bubbly Flows Encompassing Different Mechanisms. *Chemical Engineering Science* 151, 139–143.
- Rzehak, R., Ziegenhein, T., Kriebitzsch, S., Krepper, E., and Lucas, D., 2017. Unified modeling of bubbly flows in pipes, bubble columns, and airlift columns. *Chemical Engineering Science* 157, 147–158.
- Rzehak, R., Krauß, M., Kovats, P., and Zähringer, K., 2017a. Fluid Dynamics in a Bubble Column: New Experiments and Simulations. *International Journal of Multiphase Flow* 89, 299–312.
- Sato, Y., Sadatomi, M., and Sekoguchi, K., 1981. Momentum and heat transfer in two-phase bubbly flow - I. Theory. *International Journal of Multiphase Flow* 7, 167–177.
- Shawkat, M., Ching, C., and Shoukri, M., 2008. Bubble and liquid turbulence characteristics of bubbly flow in a large diameter vertical pipe. *International Journal of Multiphase Flow* 34, 767–785.
- Shi, P. and Rzehak, R., 2017. Bubbly flow in stirred tanks: Euler-Euler / RANS modeling. *Chemical Engineering Science*, submitted.
- Silva, M. K., d’Avila, M. A., and Mori, M., 2012. Study of the interfacial forces and turbulence models in a bubble column. *Computers and Chemical Engineering* 44, 34–44.
- Sokolichin, A. and Eigenberger, G., 1999. Applicability of the standard k-epsilon turbulence model to the dynamic simulation of bubble columns: Part I. Detailed numerical simulations. *Chemical Engineering Science* 54, 2273–2284.
- Speziale, C. G., Sarkar, S., and Gatski, T. B., 1991. Modeling the pressure–strain correlation of turbulence: an invariant dynamical systems approach. *Journal of Fluid Mechanics* 227,

245–272.

Tomiyama, A., Sou, A., Zun, I., Kanami, N., and Sakaguchi, 1995. Effects of Eötvös number and dimensionless liquid volumetric flux on lateral motion of a bubble in a laminar duct flow. *Proc. 2nd Int. Conf. on Multiphase Flow*, Kyoto, Japan, 3.

Tomiyama, A., Kataoka, I., Zun, I., and Sakaguchi, T., 1998. Drag coefficients of single bubbles under normal and micro gravity conditions. *JSME International Journal B* 41, 472–479.

Tomiyama, A., Tamai, H., Zun, I., and Hosokawa, S., 2002. Transverse migration of single bubbles in simple shear flows. *Chemical Engineering Science* 57, 1849–1858.

Troshko, A. A. and Hassan, Y. A., 2001. A two-equation turbulence model of turbulent bubbly flows. *International Journal of Multiphase Flow* 27, 1965–2000.

Troshko, A. A. and Hassan, Y. A., 2001a. Law of the wall for two-phase turbulent boundary layers. *International Journal of Heat and Mass Transfer* 44, 871–875.

Vieser, W., Esch, T., and Menter, F., 2002. Heat transfer predictions using advanced two-equation turbulence models. Technical report, *ANSYS Inc.*

Wallin, S. and Johansson, A., 2000. An explicit algebraic Reynolds stress model for incompressible and compressible turbulent flows. *Journal of Fluid Mechanics* 403, 89–132.

Wang, S. K., Lee, S. J., Jones, O. C. Jr, and Lahey, R. T. Jr, 1987. 3-D turbulence structure and phase distribution measurements in bubbly two-phase flows. *International Journal of Multiphase Flow* 13, 327–343.

Wellek, R.M., Agrawal, A.K., and Skelland, A.H.P., 1966. Shapes of liquid drops moving in liquid media. *AIChE Journal* 12, 854–862.

White, F. M., 1992. Viscous fluid flow. *McGraw-Hill* 2nd ed.

Wilcox, D. C., 2006. Turbulence Modeling for CFD. *DCW-Industries* 3rd ed.

Yeoh, G. H. and Tu, J. Y., 2010. Computational Techniques for Multiphase Flows — Basics and Applications, *Butterworth-Heinemann*.

Zidouni, F., Krepper, E., Rzehak, R., Rabha, S., Schubert, M., and Hampel, U., 2015. Simulation of gas-liquid flow in a helical static mixer. *Chemical Engineering Science* 137, 476–486.

Ziegenhein, T., Rzehak, R., and Lucas, D., 2015. Transient simulation for large scale flow in bubble columns. *Chemical Engineering Science* 122, 1–13.

Ziegenhein, T., Rzehak, R., Ma, T., and Lucas, D., 2017. A unified approach for modeling uniform and non-uniform bubbly flows. *Canadian Journal of Chemical Engineering* 95, 170–179.

Zun, I. 1980., The transverse migration of bubbles influenced by walls in vertical bubbly flow. *International Journal of Multiphase Flow* 6, 583–588.